Marquette University
e-Publications@Marquette

Master's Theses (2009 -)

Dissertations, Theses, and Professional Projects

Comparison of 3D Bio-Printed IPSC-CMS Derived from Healthy Donors and Patients with HLHS

Wei He
Marquette University

Follow this and additional works at: https://epublications.marquette.edu/theses_open

 Part of the Engineering Commons

Recommended Citation

He, Wei, "Comparison of 3D Bio-Printed IPSC-CMS Derived from Healthy Donors and Patients with HLHS" (2022). *Master's Theses (2009 -)*. 736.
https://epublications.marquette.edu/theses_open/736

COMPARISON OF 3D BIO-PRINTED IPSC-CMS DERIVED FROM HEALTHY DONORS AND PATIENTS WITH HLHS

by

Wei He

A Thesis submitted to the Faculty of the Graduate School,
Marquette University,
in Partial Fulfillment of the Requirements for
the Degree of Master of Biomedical Engineering

Milwaukee, Wisconsin

December 2022

ABSTRACT

COMPARISON OF 3D BIO-PRINTED IPSC-CMS DERIVED FROM HEALTHY DONORS AND PATIENTS WITH HLHS

Wei He

Marquette University, 2022

Hypoplastic left heart syndrome (HLHS) is an extremely severe form of congenital heart disease, but current treatments are not adequate. In order to find more effective treatments, we need to reproduce in vitro the physiological characteristics of cardiomyocytes associated with HLHS. Such a tissue model could be of great help to current medical research, and 3D printing technology is an effective tool for this purpose. We print layer-by-layer cardiomyocytes from both healthy and HLHS patients with laminin-based bioink to form a three-dimensional model. With our 3D cell culture technology, this model can simulate the growth conditions of cardiomyocytes in vivo. Measurements of the 3D printed samples at different time points showed that our model was able to fully demonstrate the differences between healthy and HLHS patients' cardiomyocytes. This result is the basis for more studies in the future, and we hope to build on this foundation with more diverse tests, such as drug tests, which will provide important help in the treatment of HLHS.

ACKNOWLEDGMENTS

Wei He

I would like to thank my mentors, family, colleagues, friends, and all those who have helped me. I would like to thank Jayne for teaching me how to culture and observe the cells. Thank you to Bonnie for teaching me to use the 3D printer. Thank you to Huan-Ling for helping me to collect PCR data. Thank you to Hilda for helping during the printing process. Thank you to Akankshya for agreeing and teaching me to use the program she wrote to analyze the videos. Thank you to Dr. Mike Mitchell, Dr. Aoy Tomita-Mitchell and Dr. Tefft for being my committee members and giving help and advice on the revision of the paper. Thanks also to the CTSI Traditional Pilot Award for funding. Studying alone in a foreign country is not an easy task, but all the people I met were so welcoming and I was more motivated by everyone's help and encouragement. Thank you to everyone I met and to Marquette University.

TABLE OF CONTENTS

LIST OF FIGURES

1. Introduction

Hypoplastic left heart syndrome (HLHS) is a complex congenital heart disease (CHD) that often results in severe underdevelopment of the left side of the heart. It can affect the left ventricle, aorta, aortic valve, or mitral valve. This disease accounts for most of the CHD mortality (Barron et al., 2009).

The most common treatment for hypoplastic left heart syndrome is "staged reconstruction" in which a series of procedures (usually three) is performed to reconfigure the child's cardiovascular system. The first stage is the Norwood procedure performed at birth; the second stage, the bi-directional Glenn procedure, is performed when the patient is 6 to 8 months old. The last stage, the Fontan procedure, is usually performed when the patient is 18 months to 4 years old (Best et al., 2021). This series is accompanied by a high level of risk, with the highest mortality rate being the initial procedure, with as many as three out of ten patients dying in some reported cases (Tabbutt et al., 2005). Patients who survive a complete reconstruction may also suffer from complications such as renal dysfunction, liver abnormalities, and abnormal heart rates (Feinstein et al., 2012).

Another major treatment is cardiac transplantation. However, this approach is less popular because of the scarcity of donor organs in newborns and because it has a higher mortality rate than staged reconstruction.

An in vitro disease model is important for the discovery and development of therapeutics, 3D bioprinting technology offers a way to build complex living tissues and organs. 3D printing is an important and emerging innovative technology that is widely used in industry, manufacturing, medicine and other fields. While traditional 2D printing is only on a flat surface, 3D printing not only gives shape to the material being printed but also allows precise control of the internal structure of the printed object. Bioink mixed with cells can be printed layer by layer, the same way cells are layered within tissues and organs in the human body. Many studies have begun to use this technique to construct pathological models of CHD, such as the bioengineered functional heart tissue with similar properties to natural heart tissue constructed by Zhan et al. using primary cardiomyocytes isolated from young rat hearts by 3D printing (Wang et al., 2018a).

Compared to their study, we use human induced pluripotent stem cells derived cardiomyocytes (iPSC-CMs) instead of animal cells, which makes our study more groundbreaking and innovative. iPSCs are human somatic cells that have pluripotency by reprogramming the ectopic expression of transcription factors (Park et al., 2008). iPSCs can differentiate into different cell types such as cardiomyocytes. iPSC-CMs can theoretically differentiate into the cells we need indefinitely, since the origin of these cells is often the skin or a small fraction of the blood and iPSC-CMs can show structural and regulatory elements present in a human CM, and basic functional properties of the human heart (Karakikes et al., 2015), and the genome they carry. Thus iPSC-CMs have now become an important basis for cardiovascular research.

It has been shown that cardiomyocytes differentiated from iPSC of HLHS patients can exhibit developmental and functional defects in vitro in culture, and that the gene expression causing these defects can persist in these cardiomyocytes. This supports our choice of iPSC-CM to mimic the developmental process of the hearts of HLHS patients (Jiang et al., 2014).

Cardiomyocytes grow in the human body in an environment that is not dimensionally limited, specifically, cardiomyocytes can interact with their surroundings and other cells during their development in the human body. Traditional 2D plate culture is the dominant way to culture cells in vitro, but 2D plate culture leads to two-dimensional monolayers of cells, loss of cellular interactions, and shape changes that affect gene and protein expression, and therefore, cells function differently. And we introduce 3D cell culture technology to provide a suitable microenvironment for the development of printed heart tissue. 3D cell culture systems can mimic the in vivo environment and show the cell development process (Edmondson et al., 2014a). In 3D cell culture, cells are closer to living tissues in terms of biological structure and bio-functional properties than in traditional 2D flat cell culture (Duval et al., 2017a).

In this study, we aim to construct a model that can restore cardiomyocytes in the human developmental environment and using this model we will perform a series of tests to compare the differences between bio-printed iPSC-CMs from healthy donors and HLHS patients. Thus, to further understand the etiology of HLHS patients

and the process of defective cardiomyocyte development, we hope to find inspiration in this study that will help treat or alleviate this disease.

2. Materials and methods

2.1 Bioprinter and bioink

The 3D printer (Fig.1) we use is an extrusion type commercial printer (Cellink Inkredible+). This is a common and affordable printer that has the advantage of being able to print very high-density constructs (Murphy & Atala, 2014). Extrusion printers have high compatibility in the use of bioinks, including hydrogels, microcarriers, etc. (Ozbolat & Hospodiuk, 2016). The disadvantages are the low precision and the shearing force during the printing process can break the bioink connection, but this can be restored by crosslinking the constructs after printing (GhavamiNejad et al., 2020).

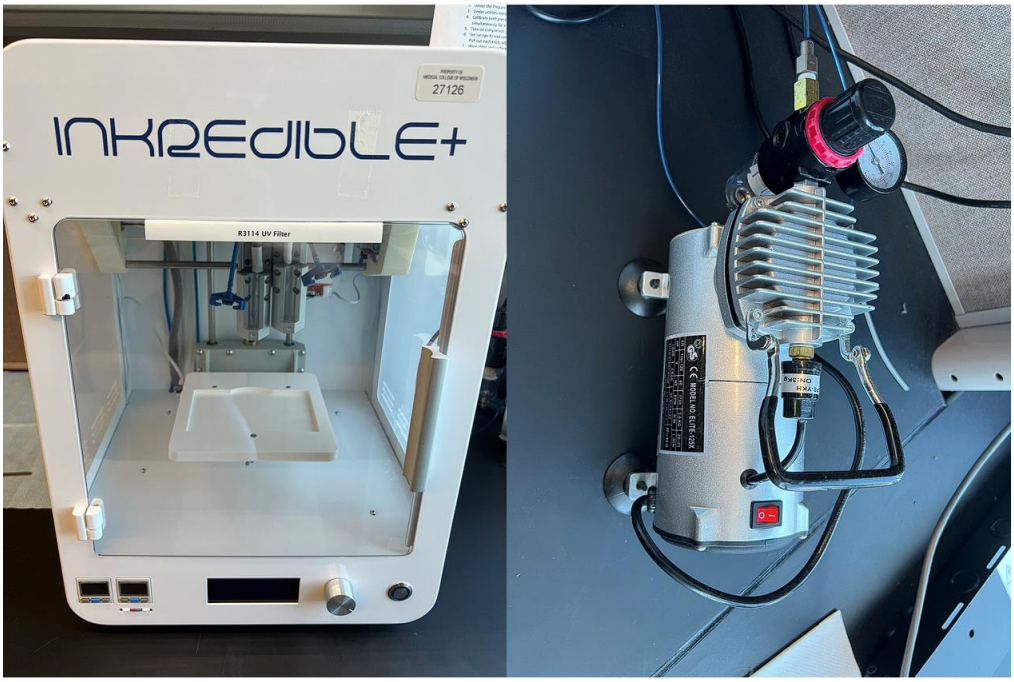

Fig.1 The bioprinter used in the experiment consists of a printer body (Left) and an air pump (Right).

2.2 Preparation of the mixture of cells

There were two sets of samples in our study, one set of tissues printed from iPSC-CMs of healthy donors called wild type, and the other set of the mixed type made from iPSC-CMs of healthy donors and iPSC-CMs of patients with HLHS in a 1:1 ratio. iPSC-CMs that had been differentiated for 15 days were washed with PBS. Cells were pre-digested with 0.25% trypsin and incubated at 37°C for 10 minutes. Cells were then collected and mixed after adding double the amount of RPMI/20% FBS solution. The mixture was centrifuged at 1000 rpm for 5 min, the supernatant was aspirated, and the cell pellet was resuspended in 0.2 ml of culture medium. 1μl of 5 μM Rock inhibitor was added to the cells and then the cells were mixed with bioink. After centrifugation for 5 min, the mixture of cells and bioink was placed in warm beads at 37°C and awaited printing.

The number of cells per print was about 1.61×10^8 and the solution volume of bioink and cells was about 1.5 ml (0.3 ml for cells and 1.2 ml for ink). Cell density is also one of the key factors in determining the success of printing. Too large a density will result in poor ink flow and printed constructs with missing shapes; too small a density will result in printed constructs with little cell content, making it difficult for the constructs to contract as a whole in subsequent cultures. After a number of experiments, we found that the density we were currently using was more suitable, and the printed constructs could maintain their shapes while there were a large number of cells in the constructs, and the constructs appeared to be beating as a whole within a week after printing.

2.3 3D bioprinting

The bioprinter was turned on and the printhead was preheated to 25°C. After first zeroing the printhead pressure, the holder was calibrated — the calibration syringe was placed into the holder and the axes were initialized, after which the holder could be set to the height we designed. To ensure that the ink was still warm, the above preparations should be done before the ink was ready.

Place the ink-filled syringe in the holder for 10 minutes to allow the 37°C to drop to 25°C because the printhead would only start working once it had reached the temperature we had set. Adjust the pressure on the printhead until the ink flowed smoothly, then select the code we programmed earlier and the bioprinter would start the printing job. The ink was extruded from the printhead and a 3-layer cube was printed on the culture plate with a volume of 4 mm × 4 mm × 0.6 mm (Fig.2). The code was set to print 4 plates at a time with a 15-second interval between plates and UV light would crosslink the printed construct during the interval. When printing was complete, the plates were sent to the cell culture hood for the next step.

During the printing process we encountered a variety of problems including the adjustment of air pump pressure, air bubbles created when the ink mixed with the cells, printing for too long resulting in lower ink temperature, etc. These problems caused our printed constructs to be too small (Fig.3) or to have a missing shape (Fig.4). We concluded the solution after several attempts, first we determined the approximate pressure range of 18-30 kPa and then adjusted the pressure in real time

during the printing process according to the ink flow rate and the shape of the printed constructs. Air bubbles in the ink had been our most troubling problem, cells and ink mixing in order to ensure uniform distribution within the solution needed to be repeatedly squeezed back and forth in two syringes, this situation was difficult to avoid the generation of air bubbles, we could only use centrifugation to reduce the impact of air bubbles. Although the printhead of the bioprinter could set the temperature, but the ink was not heated when passing through the needle, our printing was carried out in a room temperature environment, so in the case of low room temperature and long period of printing would occur in the ink cooling resulting in the needle was blocked. Our solution was to replace the needle after a round or two of printing to ensure that the ink could flow smoothly.

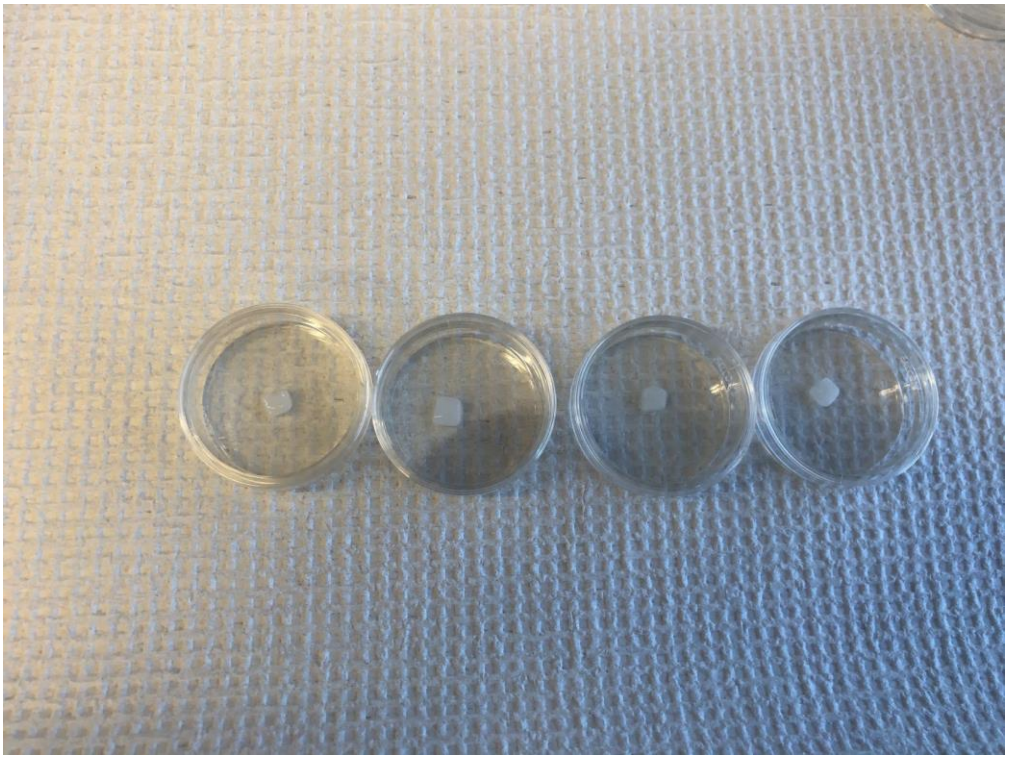

Fig.2 The constructs after one round of four prints, each construct is basically a cube.

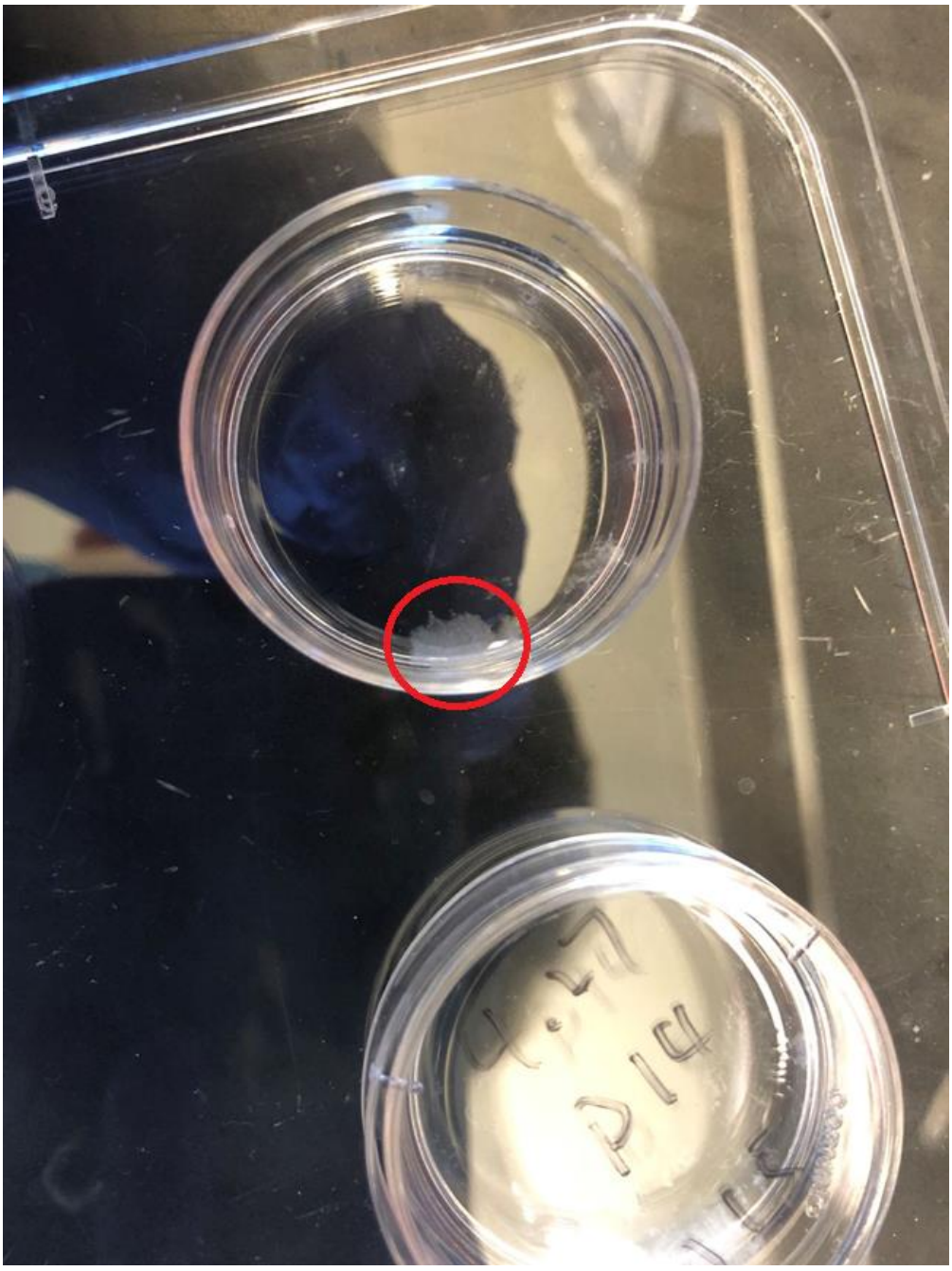

Fig.3 The red circle shows an irregularly shaped and apparently small construct.

Fig.4 A near-rectangular but slightly notched construct is shown in the red circle.

2.4 Crosslinking after 3D printing

Crosslinking plays an important role in 3D cell culture. During the crosslinking process, the cells in the printed constructs are more tightly connected and the density is enhanced therefore providing greater stability (Reddy et al., 2015). In our experience, if a construct is not fully crosslinked, it adheres to the bottom of the plate. The shape of some structures is disrupted and the cells are scattered (Fig.5). In

this case, the construct can hardly be considered "three-dimensional”, and the tissue can hardly contract even after a long period of culture. The advantages of UV light as a commonly used means of crosslinking are ease of handling and lower cost. However, if the printed construct is exposed to UV light for a long time it can cause damage to the DNA of the cardiomyocytes (Derakhshanfar et al., 2018). To reduce damage to the cells we controlled the duration of UV (405 nm) irradiation to 15 seconds, and to ensure complete crosslinking of the printed constructs, we added another crosslinking agent ($CaCl_2$ solution) on top of the UV crosslinking. Studies have shown that bioink containing calcium ions improve biological viability (Gao et al., 2017).

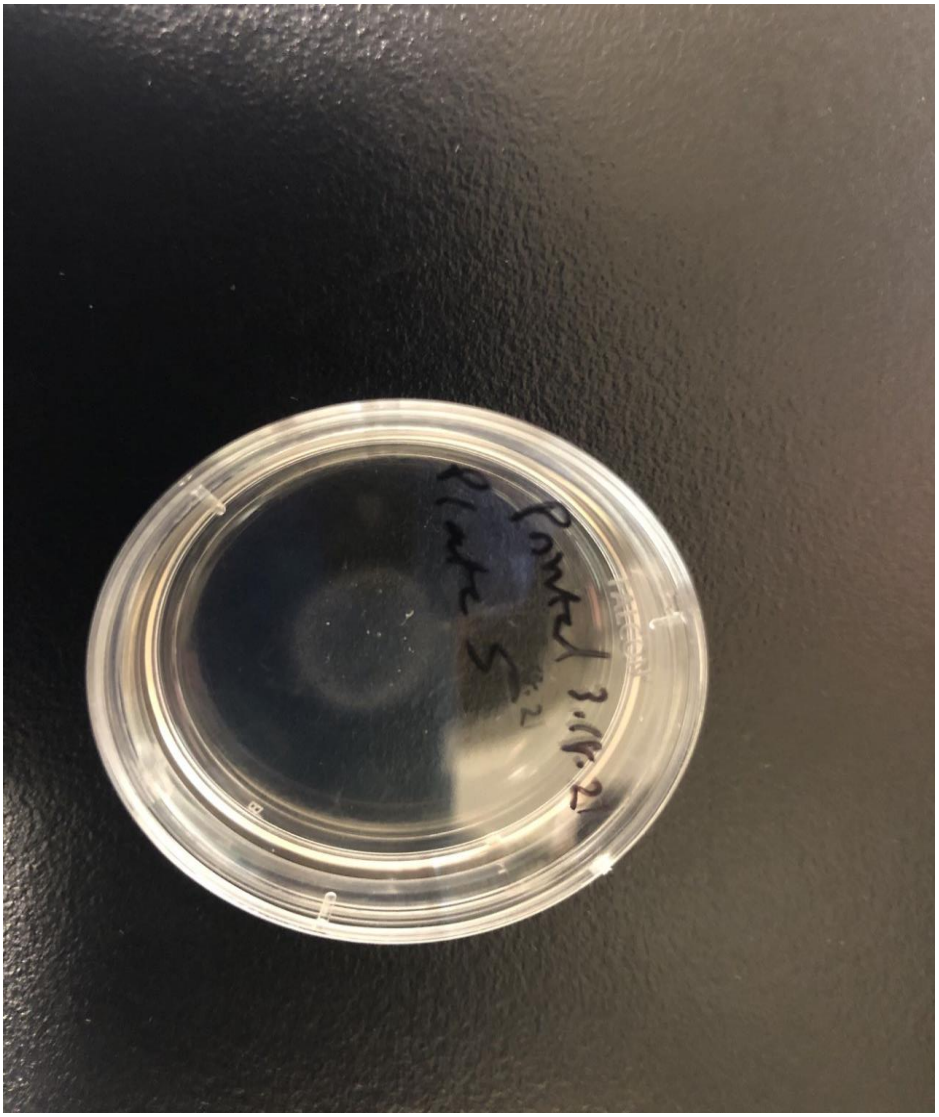

Fig.5 The figure shows a poorly crosslinked construct with cells scattered and adhering to the bottom of the plate.

2.5 3D cell culture

After soaking with $CaCl_2$ solution, the constructs were washed with PBS, and then the medium were added to the plates. We used RPMI medium with B-27 supplementation, 20% fetal bovine serum and 1× antibiotic-antimycotic. RPMI medium supports the differentiation of iPSC into cardiomyocytes, although other media such as DMEM and MEM can also promote the differentiation of

cardiomyocytes, but RPMI is more effective than these media (Lian et al., 2015). All plates were placed in a 37°C incubator and the medium were changed every three days for each plate. Despite the addition of antibiotic-antimycotic to our culture media, contamination (Fig.6) is difficult to avoid during longer culture periods, as we need to remove samples from the incubator daily for observation. Even though we have tried to avoid contamination, there are still many contaminations that make our samples are impossible to use for measurement.

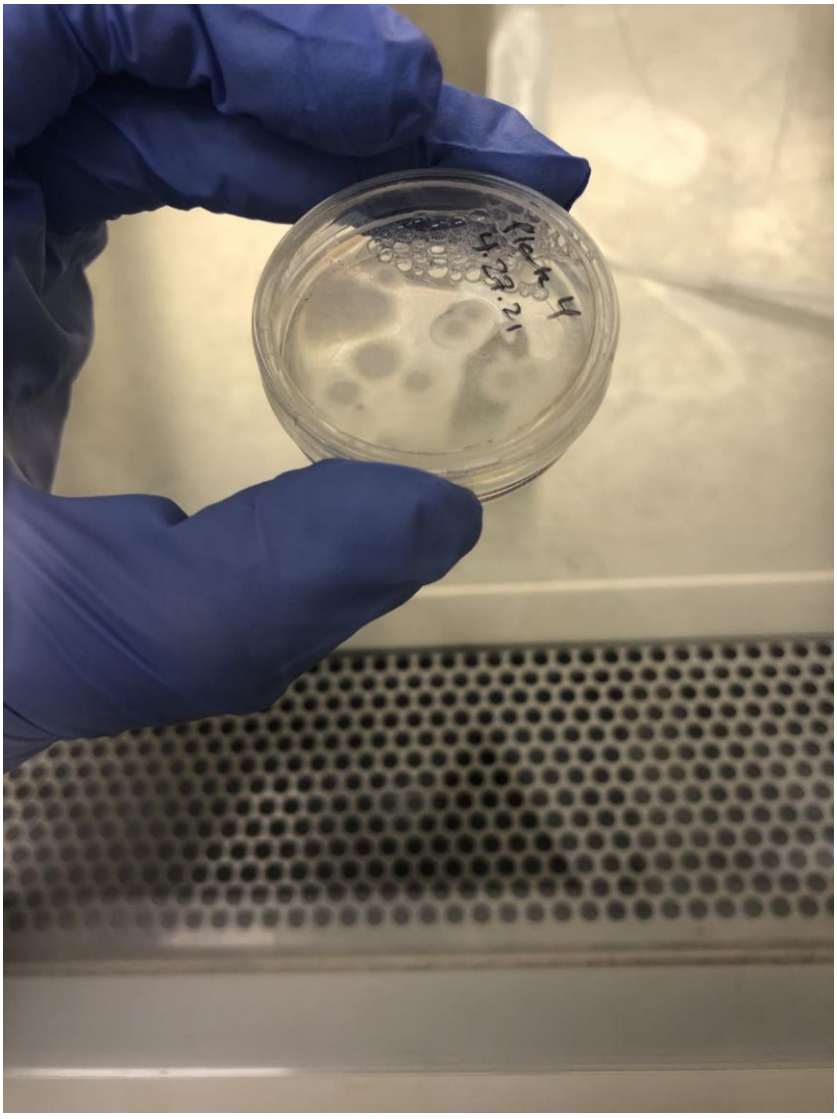

Fig.6 The figure shows a contaminated plate. It is difficult to save cells from contamination, and once contamination is present in a plate it is impossible to be used for subsequent measurements. Moreover, one plate can contaminate other plates nearby overnight and we have to clean the whole incubator, which affects the progress of the whole experiment.

2.6 Observation and recording

Each sample was observed and recorded under the microscope daily. The microscope eyepiece was 10× and photographs and videos were taken under objectives 4×, 10×, and 20× (only the 100× videos were used to analyze). The video format was 2880×2600 with 5 frames per second. The photo format was 2880×2200, and a scale bar was set up in the photos. Photographs and videos taken on the same day belonging to the same sample were used to calculate the contraction velocity and displacement of the bio-printed tissue at the point in time we had set (every 5 days). Photographs with scale bar were imported into ImageJ to calculate the pixel length scale, which was used to calculate the pixel displacement distance in the video analysis program.

We used a MATLAB program (Shradhanjali et al., 2019) for video analysis to measure the displacement of tissue due to contraction in the video. The program would automatically calculate the displacement of the pixels in each frame and obtain the maximal averaged displacement based on the average of the displacements of all pixels. Also since the video is 5 frames per second and the timestep of a frame is 0.2 seconds, dividing the maximal averaged displacement by 0.2 will give the maximal averaged contraction velocity.

The program utilizes the Adaptive Reference-Digital image correlation (AR-DIC) method to continuously adjust the adaptive reference frame so that the displacement occurring during the spontaneous contraction of the cardiomyocyte is correctly quantified. Shown in Fig.7 (a) is a frame from a video (video taken under a microscope at 100× magnification) of the contraction of the 3D printed construct, and in Fig.7 (b) is a pixel map of the contracted construct captured by the program using AR-DIC. The program compared all the displacements of each pixel point from the initial position to the one produced by the construct contraction, then selected the maximal displacement of each pixel point from all the displacements and divided the maximal displacement of all the pixel points by the number of all the pixel points after accumulating them to obtain the maximal averaged displacement.

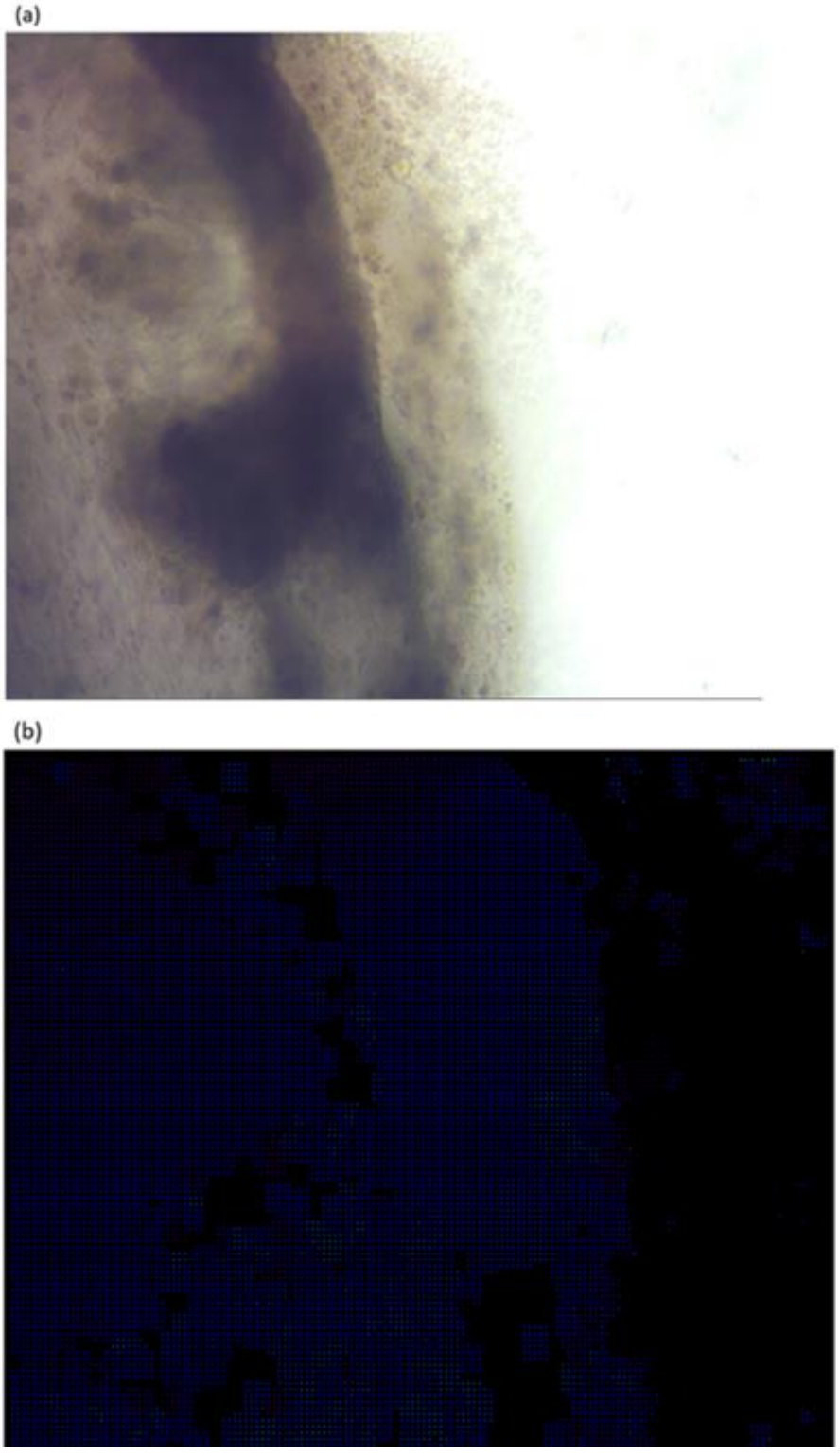

Fig.7 The maximal averaged displacement resulting from the contraction of the construct was analyzed using the MATLAB program. (a) A frame from a video of the contraction of the wild type after 20 days of culture (video taken under a microscope at 100× magnification); (b) pixel map of the contracted construct captured using the AR-DIC method of the program.

2.7 Immunofluorescence

The sample collection time points established for our study were days 5, 10, 20, and 30 (after printing), and when this time point was reached, samples with less contraction among wild type and mixed type were selected for the collection. We did this because in our experience samples that contract less or even stop contracting had often begun to apoptosis and would not return to viability even if the tissue continued to be cultured. To ensure that there were still samples that were still contracting at subsequent time points, we must prioritize the collection of less viable samples.

The collected samples were fixed by aspirating the culture solution and rinsing three times with PBS solution, adding 4% PFA solution, and shaking at -4°C for 15 minutes. The samples were then permeabilized by adding a mixture (primary antibody solution) of GATA4, α -actinin, and PBS (1:400 for GATA4 and 1:250 for α -actinin) and shaken overnight at 4°C. After removing the primary antibody solution and rinsing five times with PBS, the secondary antibody solution was added and shaken for one hour at room temperature, with the primary components of 2° GATA4 (donkey anti-Rabbit Alexa Fluor 594), 2° α -actinin (goat anti-Mouse IgG1 Alexa Fluor 488), DAPI and PBS. The ratio of all three secondary antibodies was 1:750. After thoroughly washing off the secondary antibodies with PBS solution, the samples were mounted on coverslips with Prolong Gold Antifade Reagent (Molecular Probes™).

Samples were photographed at 630× magnification (Fig.8) under a confocal microscope (Zeiss). The resolution of the photo with the scale bar is 673×673. Import

the image with the scale bar into ImageJ and measure the length of each pixel with the scale length. As shown in the figure below, drag and drop the image you want to measure into ImageJ, select 'Straight' in the toolbar, then enlarge the scale as shown in Fig.9 (b) and draw a horizontal line from the head to the end of the scale bar with the mouse pointer. Then go back to the toolbar and select 'Analyze' and select 'Set Scale' in the drop-down menu. At this point, ImageJ will pop up the same interface as Fig.9 (c), 'Distance in pixels' indicates the length of the drawn line in pixels. In the 'Known distance' column, fill in the actual length of the scale bar, and then change the units in the 'Unit of length' column to the units of the scale bar. The 'Scale:' column below shows the conversion relationship between the pixel length and the actual length in this image. For example, Fig.9 (c) shows 16.2 pixels/μm, which means that one micron is equal to 16.2 pixels in this image. In other words, the actual length of one pixel is about 0.062 microns.

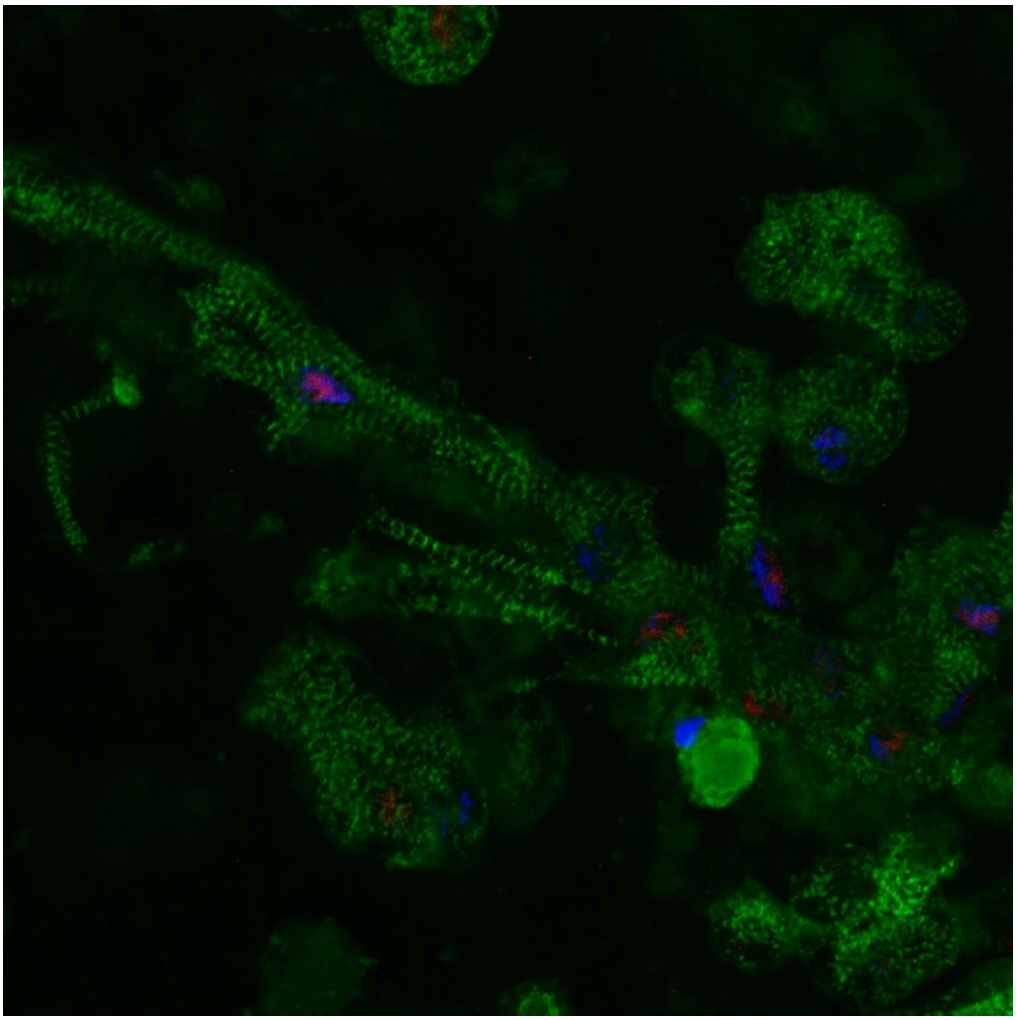

Fig.8 Pictures taken after immunization fluorescence under a confocal microscope at 630× magnification. Red, GATA4. Green, α-actinin. Blue, DAPI.

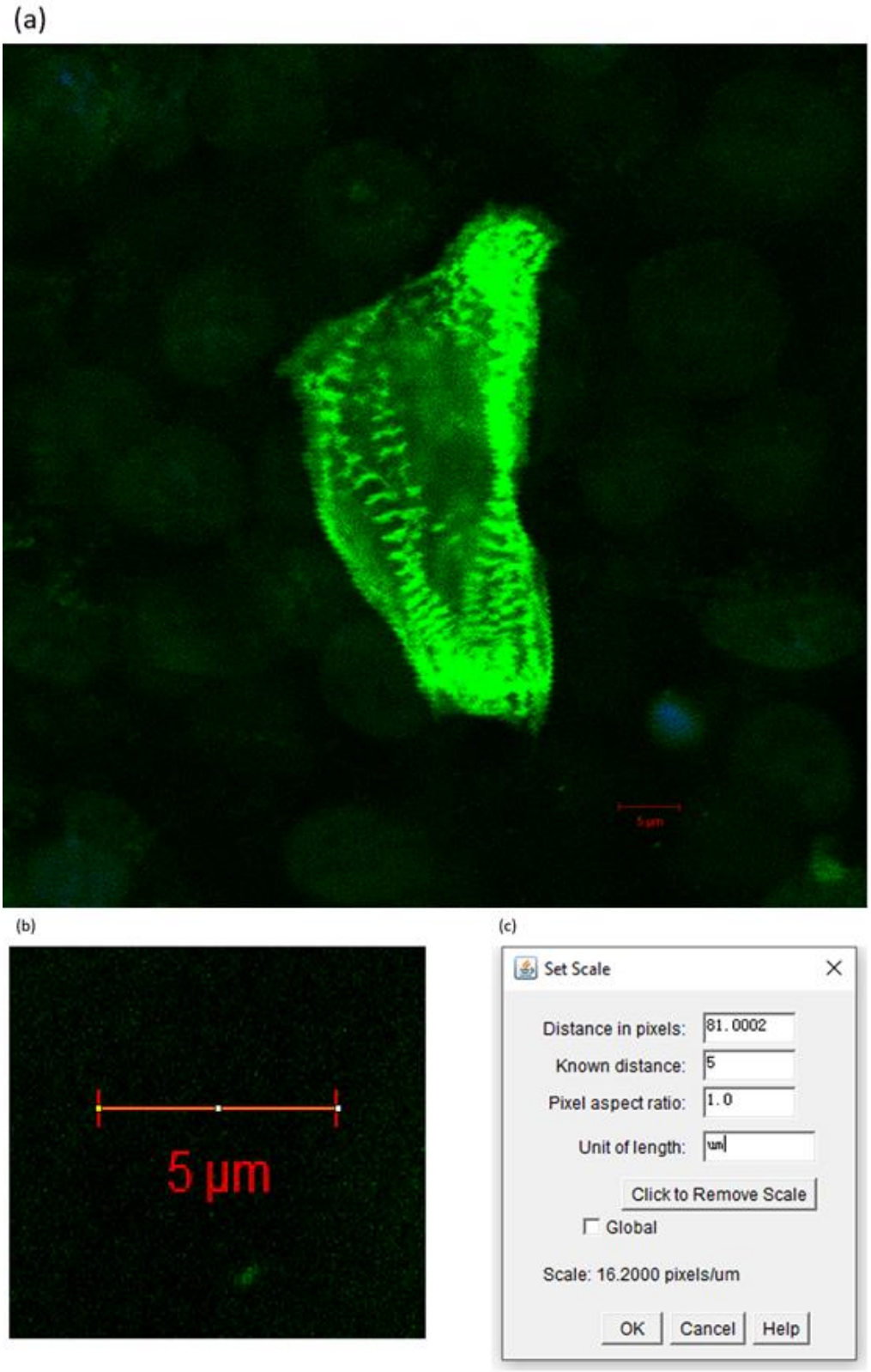

Fig.9 Measure the actual length of pixels in an image using ImageJ. (a) image after immunofluorescence of wild type after 10 days of culture (image taken under a confocal microscope at 630× magnification) with a scale bar length of 5 μm; (b) select 'Straight' in ImageJ and draw a horizontal line on the magnified scale bar; (c)

select 'Analyze' and 'Set Scale' in the toolbar and enter the actual length and unit of the scale bar, which is converted to obtain the length of individual pixel of the image.

Import the image with scale bar into ZEN software (3.4, blue edition), frame the area of interest (perpendicular to the direction of the sarcomere alignment) and the software will export the densities between each sarcomere (in pixels). Multiply the pixel length by the ratio derived with ImageJ to get the sarcomere length. The lengths obtained for multiple photos belonging to the same sample were averaged for comparison in this study.

As shown below (Fig.10), drag and drop the same image which derived actual pixel length using ImageJ into ZEN, select 'Profile' in the left toolbar, and then select the Rectangle tool in the bottom toolbar. Zoom in on the area you want to measure in the image bar, draw a rectangle in the area, and note that the center line of the rectangle needs to be perpendicular to the direction of the sarcomere alignment (Fig.10 (c)). The tool will automatically check the intensities of each sarcomere within the rectangle and display them in summary on the left side of the image (Fig.10 (b)). Since we are using the trial version, we need to manually calculate the pixel distance between each peak of the left image and multiply it by the ratio derived with ImageJ to get the actual sarcomere length.

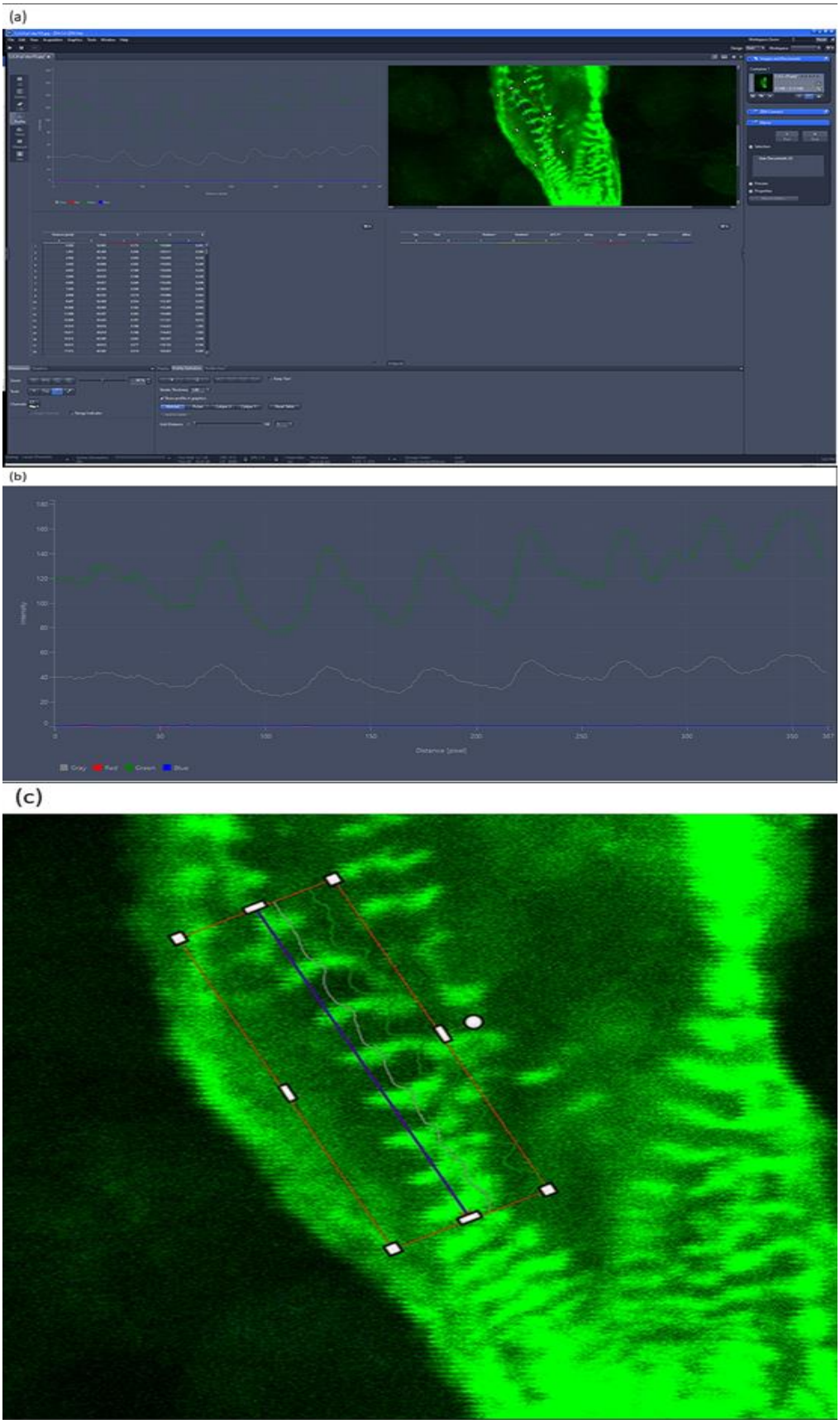

Fig.10 Calculate the sarcomere length using ZEN software. (a) The interface of ZEN software; (b) The image on the left side at the top of the interface,

summarizing the intensities of the sarcomeres within the rectangle tool, calculating the pixel distance between each peak and multiplying it by the actual pixel length derived previously to obtain the sarcomere length;(c) Zoom in on the area of interest with the center line of the rectangle tool perpendicular to the direction of the sarcomere alignment.

The resolution of the images without scale is 2048×2048 and these photos were used to analyze the organization index. We chose to use the organization index to quantify the alignment of sarcomeres in the samples.

This is done by importing the original color image into ImageJ, separating the colors (Fig.11 (a)), and converting the image with sarcomeres to binary (Fig.11 (b)). Select 'Grid' in the toolbar (Fig.11 (c), for our experiments we chose the default size (Fig.11 (f)). Using the grid as a unit, zoom in on the grid (Fig.11 (d)) you want to measure and use the 'Straight' tool to draw a straight line through the sarcomeres. Hold down the 'ctrl' and 'K' keys on the keyboard at the same time to get the distribution of the intensities of the sarcomeres in the grid (Fig.11 (e)) and import the data into the MATLAB program to get the sarcomere organization index in the grid. The global organization index can be calculated by importing the data of multiple grids into the program at the same time (Fig.11 (g)), and then the organization index of multiple images of the same sample can be averaged to obtain the organization index of the sample.

The organization index of the image was obtained by measuring the intensities of the sarcomeres in each grid and then using MATLAB to perform FFT (Hinson et al., 2015) on the intensities. The organization index of multiple images belonging to the same sample was averaged, and then the organization index of all samples was

then listed together, and all values are normalized by the maximum value (Deacon et al., 2019).

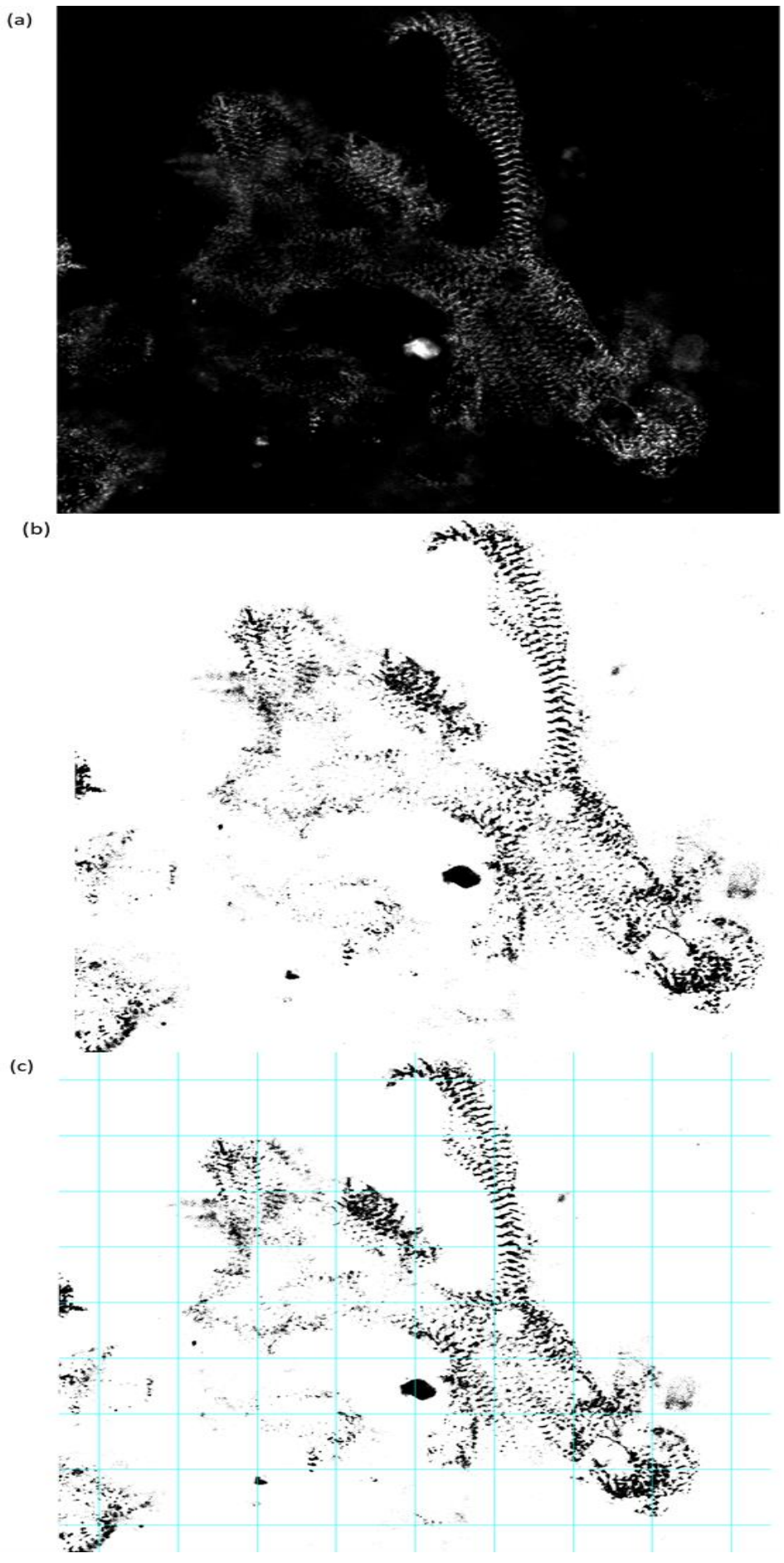
(a)
(b)
(c)

(d)

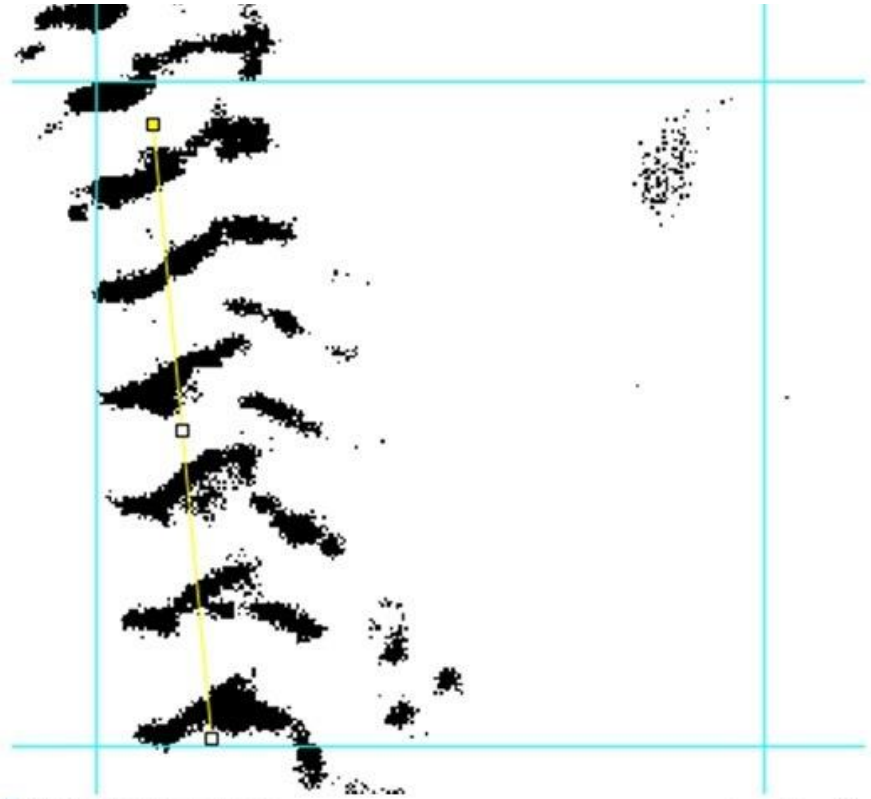

(e)

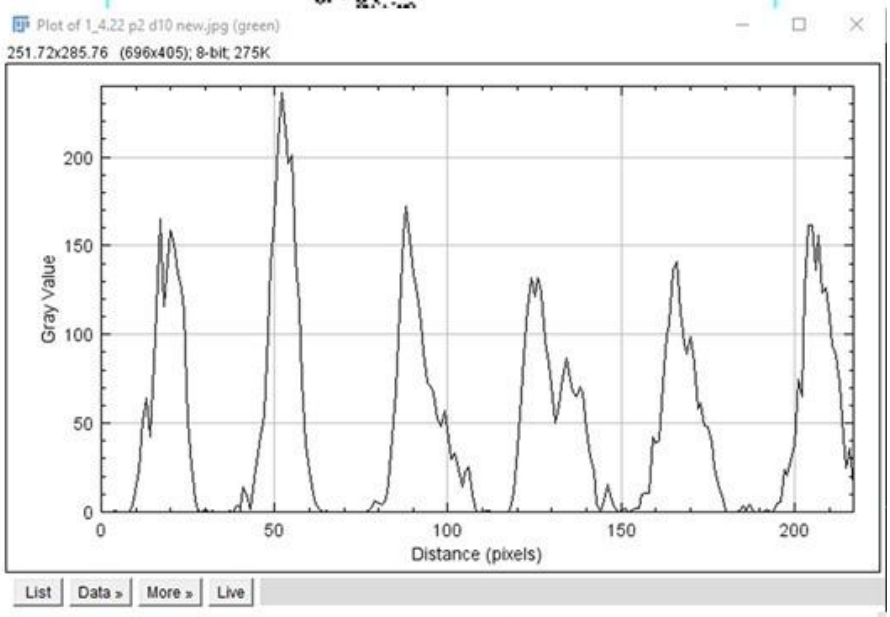

(f)

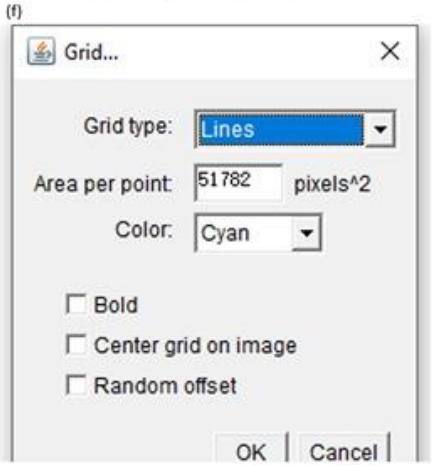

(g)

```
org =

    0.1064
    0.0172
    0.0252
    0.0316
    0.0234
    0.0480
    0.0294
    0.2837
    0.3679
```

Fig.11 Calculation of sarcomere organization index using ImageJ and MATLAB. (a) Color differentiate the colored images (similar to Fig.8) to keep only the parts containing sarcomeres; (b) Binary conversion of the resulting image; (c) Lay the grid on the converted image, we use the default size grid (f); (d) Using the 'straight' tool to draw a straight line through the sarcomeres in the grid where the measurement is desired; (e) Hold 'ctrl' + 'K' to obtain the distribution of sarcomeres intensities within that grid; (g) Repeat steps (c), (d) and (e) to get the data of intensities distribution of all grids of the image and import into MATLAB to get the organization index of the image.

2.8 RT-qPCR

The sample collection time points were the same as the immunofluorescence. Two samples from each group were picked, the medium was washed off with PBS and stored at -80 degrees Celsius. We purified the samples with RNeasy Plus Micro Kit (Qiagen).

We used 1.0 μg of total RNA for cDNA synthesis (Qiagen QuantiTect RT Kit). Thaw all reagents on ice and flick each tube to mix. Quickly centrifuge all reagents to bring the residue to the bottom of the tube. Prepare the gDNA elimination reaction on ice, then incubate at 42 degrees C for 2 minutes and immediately place on ice. Prepare the reverse transcription master mix for each tube on ice. Add the template RNA to each tube containing the RT master mix. Incubate at 42 degrees C for 30 minutes to increase cDNA yield and at 95 degrees C for 3 minutes to inactivate the enzyme. Place the RT reactions on ice and perform RT PCR directly or store the reactions at -80 degrees.

Set up the RT-PCR reaction master mix according to the following recipe: Taqman master mix, target 1 (GADPH) and target 2 (one of the genes we want to

detect), ROX (for Roche master mix only), and nuclease-free water. Add 1× Taqman master mix to a 384-well PCR plate, 4 ul per well, in triplicate for each assay. Add 1ul of diluted cDNA to each well containing Taqman master mix. Seal the plate with microseal film. Run QuanStudio real-time PCR using the comparative CT (Delta Delta CT) method: 50°C for 2 min, 95°C for 10 sec, then 95°C for 15 sec, and 60°C for 1 min for a total of 40 cycles. Analysis was performed using gene expression format.

3. Results

3.1 Culture outcomes

Most of our samples of wild type started contracting on Day 3-5 after printing while the mixed type trend started contracting later than the wild type, usually on Day 5-7 after printing. There was also a contract area difference between the two groups, the samples in the wild type usually had a greater contract area (Fig.12) than those in the mixed type (Fig.13). Moreover, the samples in the wild type contracted as a whole while onlwy a partial area of the samples in the mixed type contracted.

The comparison between the Fig.12 and Fig.13 images shows that the cells in the wild type were more tightly connected to each other, while in the mixed type of construct there is significantly smaller and less tissue formed by cell connections. There were many tiny black dots in the areas of the mixed type of samples that were not connected, and we suspected that these were apoptotic cells, but we did not measure the cell survival rate. We plan to include survival measurements in our next experiments.

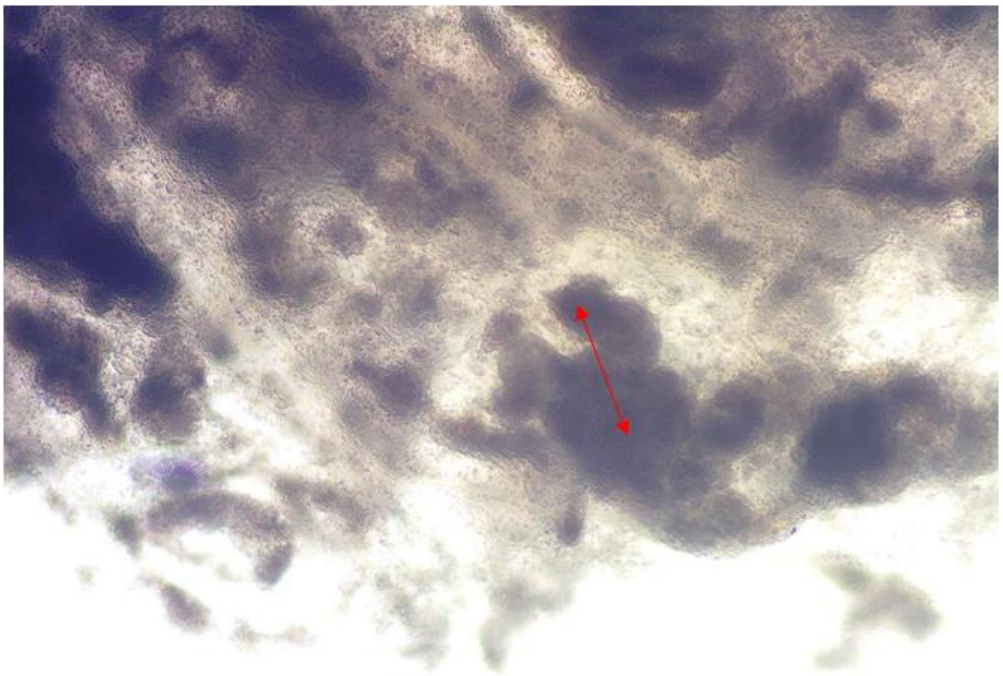

Fig.12 The figure shows the construct from wild type under a 40× microscope, the photo was taken 20 days after printing, and the whole construct contracts monolithically along the arrow direction.

Fig.13 The image shows the culture of the mixed type at 20 days after printing. The circle shows the contracted part of the construct visible in this area after 40× magnification.

3.2 Video analysis results

We chose the same parameters in our MATLAB program for all the videos we wanted to analyze. We chose the 100× videos to do the measurements because they have more detail than the 40× videos and a better field of view than the 200× videos. Not all videos were analyzed, and we selected the samples with the longest culture times, which had recordings of all time points.

The program was designed to calculate the pixel intensity changes for each frame in the video. The intensity changes would be used to calculate the displacement of the tissue in the video.

Our results are shown in Fig.14, where the maximal averaged displacement of mixed type did not show a linear increase with culture time, reaching a maximum on Day 10 then decreasing but increasing again on Day 25 (Fig.14(a)). In Fig.14(b), the maximal averaged displacement of the wild type showed a slow increase with culture time, with the maximum value occurring on Day 30, while at the first measurement time (Day 5) the wild type showed a displacement close to the maximum value in the mixed type. In the comparison between the two groups (Fig.14(c)), significant differences were observed on Day 5, 20 and 30, wild type exhibits greater contraction displacement.

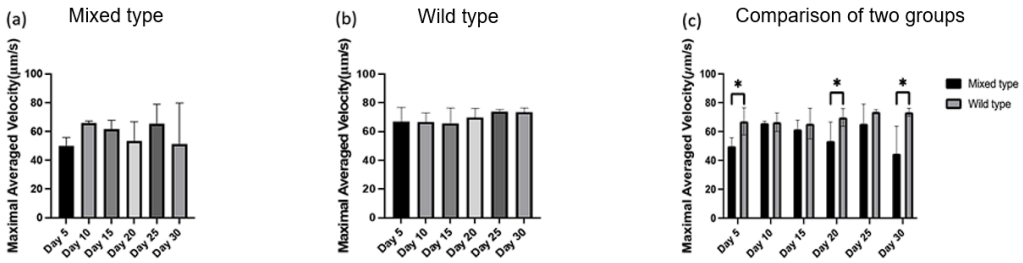

Fig.14 Comparison of the maximal averaged displacement of the two groups of samples at different time points. (a) shows the mixed type, the displacement of this group of samples did not increase gradually with the culture time, and the maximal displacement appeared on Day 10. In (b), the displacement of the wild type reached the maximum value of the mixed type on Day 5, and it did not increase sharply in the next culture period but also increased slowly with time. (c) Comparison of the displacements of the two groups of samples at different time points, showing significant differences on Day 5, 20 and 30 ($p<0.05$).

The measurements of the maximal averaged contraction velocity for both groups are shown in Fig.15. Since we kept the parameters the same when we shot the video therefore the timestep of each frame of the video is the same 0.2 seconds. And the way we calculate the contraction velocity was simply the displacement divided by the time, so our results about the maximal contraction velocity are proportional to the maximal displacement. Mixed type samples show a significant increase in contraction velocity at the beginning of the culture, but a decrease at Day 15 and 20 and another increase at Day 25. The wild type samples show a slow increase from the beginning to the end of the culture. There is a significant difference between the two groups of samples in the measurements on days 5, 20 and 30. Day 20 and 30 are both the time points when the samples of the mixed type show a decrease in contraction velocity.

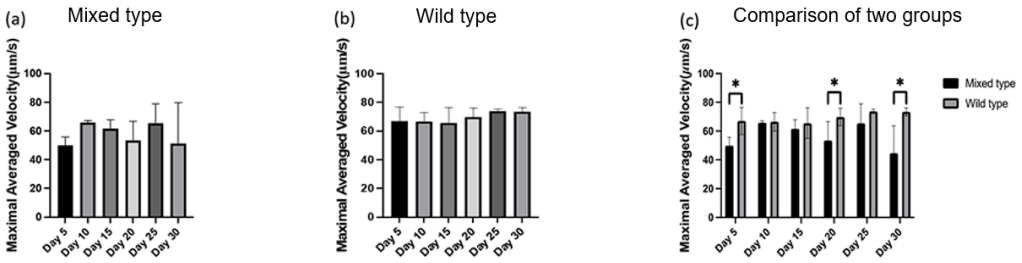

Fig.15 Comparison of the maximal averaged velocity of the two groups of samples at different time points. We used the same video specifications for filming each frame of each video so the timesteps are consistent, the differences show here are the same as Fig.14. The mixed type in (a) has no linear relationship with the maximal velocity on Day 10. The wild type in (b) increases slowly with culture time, with the maximum value at Day 30. In (c), the two groups of samples show significant differences ($p<0.05$) on Days 5, 20 and 30.

3.3 Sarcomere length

The two groups of samples realized a huge difference after staining, where sarcomeres were abundant and clearly visible in the wild type, but very few and faint in the mixed type. Even in the early mixed samples, sarcomere was not found at all, so it led us to not have enough data. In Fig.16, we show two samples on Day 20 after fluorescence staining, (a) the sample of wild type and (b) the sample of mixed type, and the difference is obvious. In (a), the wild type shows sufficient sarcomeres and is very clear and has some alignment. In (b) it is difficult to find sarcomeres, which are hidden in a cell and are not only very faint but also scarce.

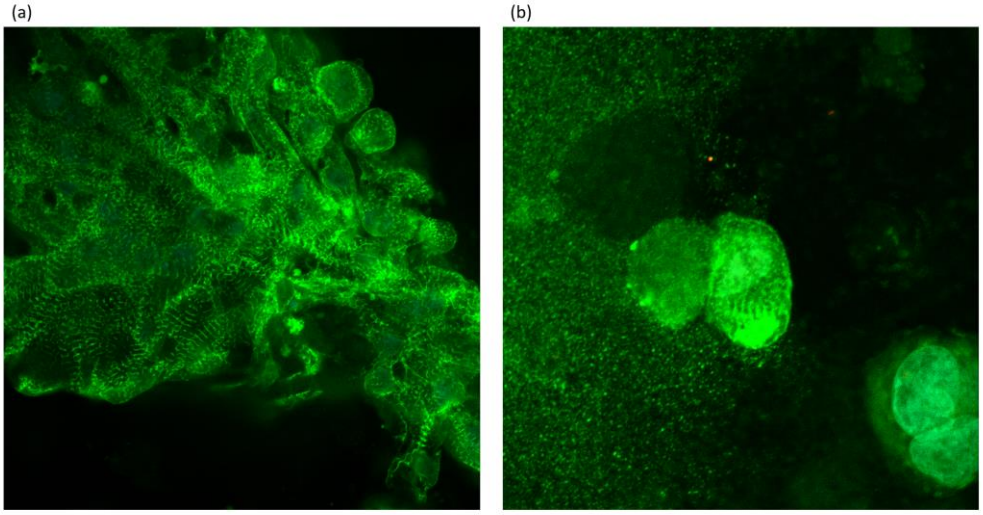

Fig.16 Pictures of sarcomeres observed under a 630× confocal microscope after fluorescence staining of the samples on the Day 20 after printing. Comparing the wild type (a) with the mixed type (b), we can easily see that there is a significant difference in sarcomere clarity and alignment between the two. In (b), the sarcomeres of the mixed type show only a few faint strips in one cell, while the sarcomeres of the wild type in (a) are not only numerous but also very clear and has alignment.

The mixed type has the minimum sarcomere length on Day 5 and the maximal length on Day 10 (Fig.17 (a)). The maximal length is 1.63 μm, corresponding to the length of early sarcomere length of 1.6 μm in other studies (Lundy et al., 2013; Yang et al., 2014). After Day 10, the sarcomere length decreased but was still higher than the value on Day 5. Measurements of the mixed type were more difficult than those of the wild type because it was difficult to observe clear sarcomeres in the early samples of the mixed type than in the wild type, and because we collected only two samples at each time point, there were insufficient data because sarcomeres were not observed in some samples. Also, we did not have data for Day 30 because our samples were contaminated before Day 30 and no clear sarcomere was observed in the collected samples.

The wild type shows a linear increase in sarcomere length, with significant differences between Day 5 and other time points (Fig.17 (b)). After Day 5, the wild type shows no significant differences in sarcomere length. The maximal sarcomere length appears on Day 30 as 1.99 μm, which is close to the length of mature sarcomeres mentioned in other studies of about 2 μm (Lundy et al., 2013; Yang et al., 2014). In the comparison of the two data sets (Fig.17 (c)), only a significant difference is observed on Day 20.

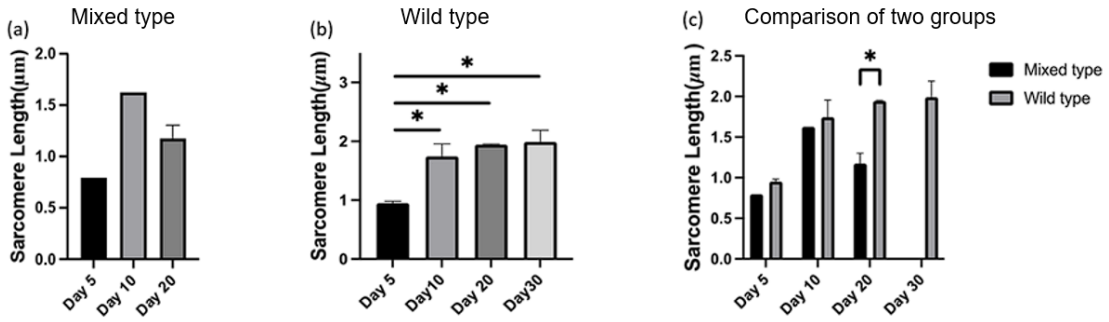

Fig.17 Comparison of the sarcomere lengths of the two groups of samples at different time points. (a) The mixed type is shown to have the maximal sarcomere length on Day 10, with a maximum value of about 1.6 μm. (b) The sarcomere length of the wild type has a slow increase with time, with the maximum value occurring on Day 30 and being about 2 μm. The sarcomere length on Day 5 shows significant differences from other time points ($p<0.05$). In the comparison of the two groups of samples (c), since we did not have enough data for the mixed type, we could only find a significant difference between the two groups on Day 20 ($p<0.05$).

3.4 Organization index

The sample of the mixed type has data for only three time points (one at each time point) due to insufficient sample, with the maximum value occurring on Day 10 and the minimal value on Day 20 (Fig.18 (a)) while the samples of the wild type show a linear increase at the first three time points, but a small decrease at the last time

point. The maximum value appears on Day 20 and the minimal value on Day 5 (Fig.18 (b)). The mixed type does show a lower average organization index at each time point, but additional samples are needed to confirm the observation (Fig.18 (c)).

Reviewing the measurements of maximal displacement and velocity and sarcomere length, there is some consistency across time points for all measurements in the wild type. Specifically, there is an increasing trend in the first 30 days, with a significant difference in wild type sarcomere length between Day 5 and Day 10, 20 and 30, which is not reflected in the results for maximal displacement and velocity of contraction.

The mixed type shows a maximum in displacement, velocity, and sarcomere length results on Day 10, follows by a decrease in all measurements, reaching the first underestimation of its growth phase at Day 20. It is reasonable to assume that the mixed type has 50% of cardiomyocytes with HLHS and that these cells stop growing or even show apoptosis after 20 days of culture, which leads to a decrease in the upward trend that should occur in the growth phase of the whole construct.

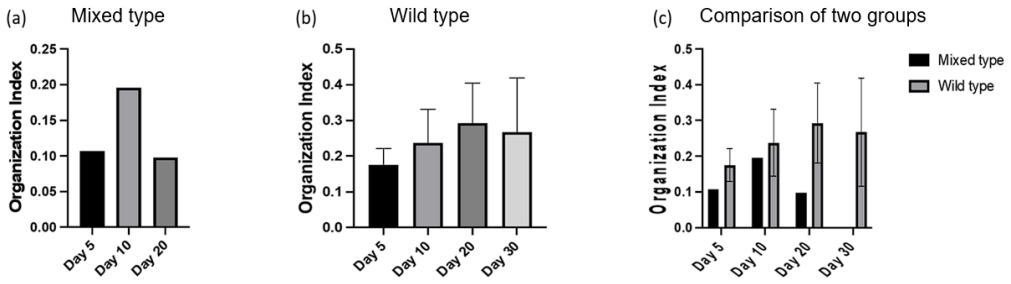

Fig.18 Comparison of the organization index of the two groups of samples at different time points. All sarcomere organization indices were normalized to the highest recorded value, such that the reported tissue index is a value between 0 and 1. The sarcomeres of mixed type (a) have the maximum value on Day 10. The wild type

in (b) increases slowly with time but decreases on Day 30, so the maximum value occurs at day 20. In (c) we were not able to show whether there is a significant difference between the two groups because we did not have enough data on the mixed type.

3.5 Wild type grows faster than mixed type

Gene expression in both sets of samples showed significant differences between conventional 2D culture compared to the combination of 3D printing and 3D cell culture, as well as dramatic differences between wild type and mixed type after the same printing and culture.

It is important to note that since the 2D samples did not undergo the printing step, the post-differentiation times are used uniformly in all subsequent comparisons that include 2D samples. Another point to note is that the 2D samples do not have a mixed type, but a variant type instead. The difference between the two is that the mixed type contains half of the diseased cardiomyocytes and the normal healthy cardiomyocytes, whereas the variant type contains only diseased cardiomyocytes.

ACTA1 is responsible for encoding skeletal muscle α-actin, which plays a crucial role in muscle movement and contraction(Laing et al., 2009). But *ACTA1* tends to be abundantly expressed in humans early in embryonic development, declines in mid-to-late development and reaches negligible levels by the time the infant is born (Ilkovski et al., 2005). As seen in Fig.19, the samples are stressed after 3D printing and express higher *ACTA1* levels, but this level becomes normal over time. Comparing the wild type (3D wild type Day 16 was used as control) and mixed type in 3D it is not difficult to find that the decrease of *ACTA1* from Day 16 to Day 20

(after differentiation) in the wild type is much higher than that in the mixed type, and we speculate that the wild type has a faster developmental rate than the mixed type.

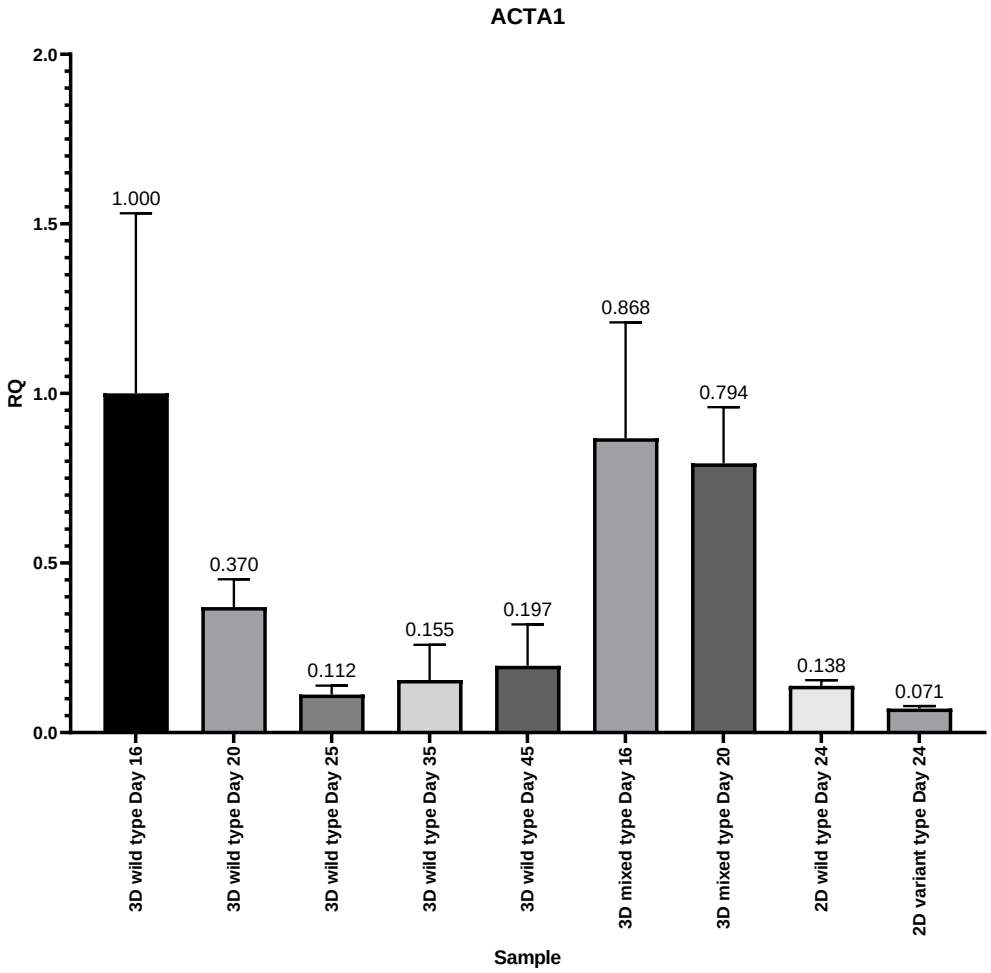

Fig.19 Comparison of *ACTA1* expression in 2D and 3D samples at different time points. *ACTA1* is abundantly expressed at the early stage of cardiomyocyte development and gradually decreases with development. In the figure, it can be seen that the decreasing trend of *ACTA1* is more obvious in 3D wild type than 3D mixed type, which indicates that wild type develops more rapidly than mixed type.

MYL2 has an important role in cardiac contractile function during early embryonic development (Sheikh et al., 2015). The expression of 3D printed and cultured wild type gradually increases over time (Fig.20), suggesting that 3D printed

cardiomyocytes have a more rapid maturation rate and cardiomyocytes are developing from atrial like to ventricular like.

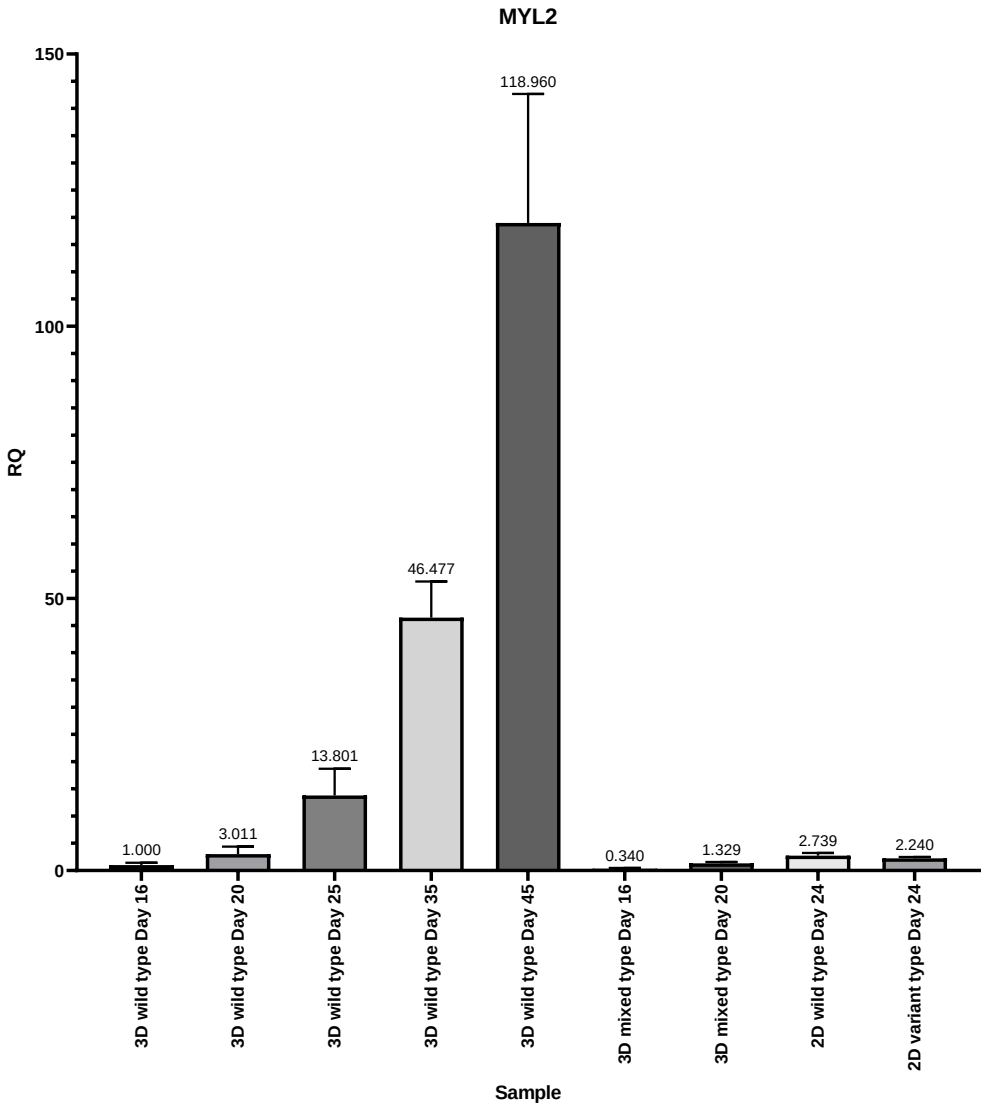

Fig.20 Comparison of *MYL2* expression in 2D and 3D samples at different time points. The expression of *MYL2* in the 3D wild type increases rapidly with culture time, showing that the wild type has a faster maturation rate than the 3D mixed type, and the cardiomyocytes are developing from atrial to ventricular shape.

SLN expression determines muscle relaxation function (Tupling et al., 2011), but overexpression of *SLN* leads to reduced contractility in cardiomyocytes (Babu et

al., 2005), so the expression of *SLN* decreases gradually with developmental time. The mean value of *SLN* expression in 3D wild type shows a decrease, but the variance is high, more samples are needed to improve that expression of *SLN* would decrease from the early development in the 3D wild type. The 3D mixed type shows an increased *SLN* expression even after 5 days of culture and there is a gradually decreased *SLN* expression after Day 20 in wild type (Fig.21). Therefore, we speculate that the wild type has a stronger contraction capacity than the mixed type.

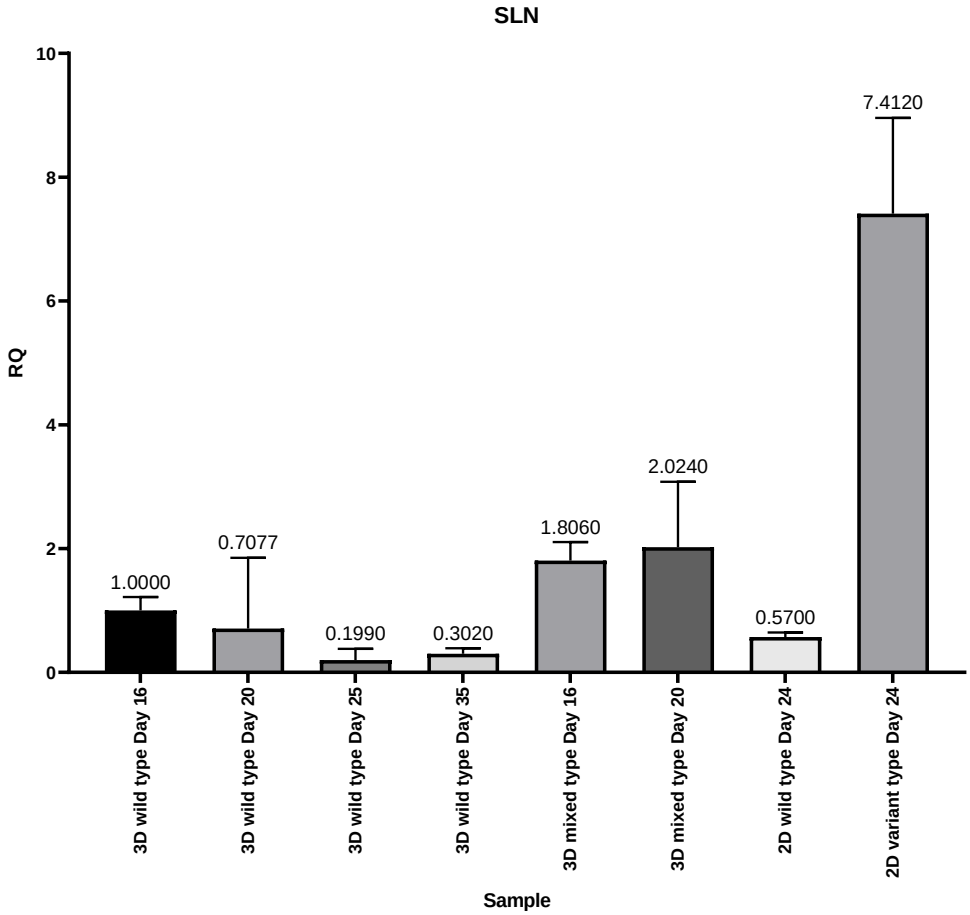

Fig.21 Comparison of *SLN* expression in 2D and 3D samples at different time points. The expression of *SLN* decreases gradually with cell development, and it determines the contractile ability of cardiomyocytes. *SLN* decreases gradually with culture time in 3D wild type but increases in 3D mixed type. Based on this, we

speculate that wild type has a stronger contractile capacity than mixed type. And more samples are needed to confirm this.

BIN1 is a tumor suppressor protein (Sakamuro et al., 1996), from our results (Fig.22) it appears that 3D printing do not have a dramatic effect on the expression of BIN1.

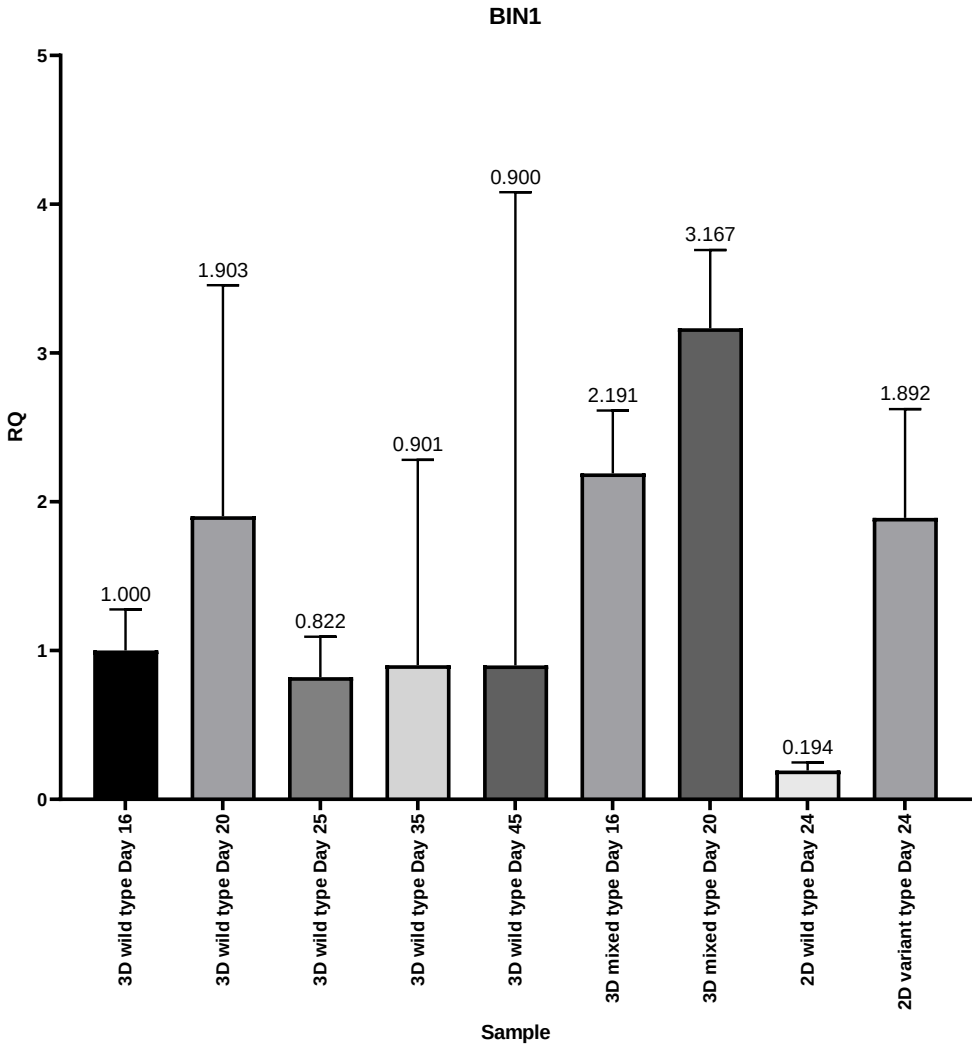

Fig.22 Comparison of *BIN1* expression in 2D and 3D samples at different time points. 3D printing does not have a significant effect on *BIN1* expression.

JPH2 plays a key role in promoting intracellular calcium release and cardiac contraction (Landstrom et al., 2007). In Fig.23, the 3D printed samples express much higher levels than the 2D samples, and there is also a large difference between the wild type and the mixed type. There is a significant difference ($p<0.05$) between Day 16 and Day 20 in the 3D wild type, but not in the mixed type, showing that 3D wild type has a faster developmental rate. Studies have shown that hypertrophic cardiomyopathy is associated with downregulation of JPH2 (Landstrom et al., 2011) .

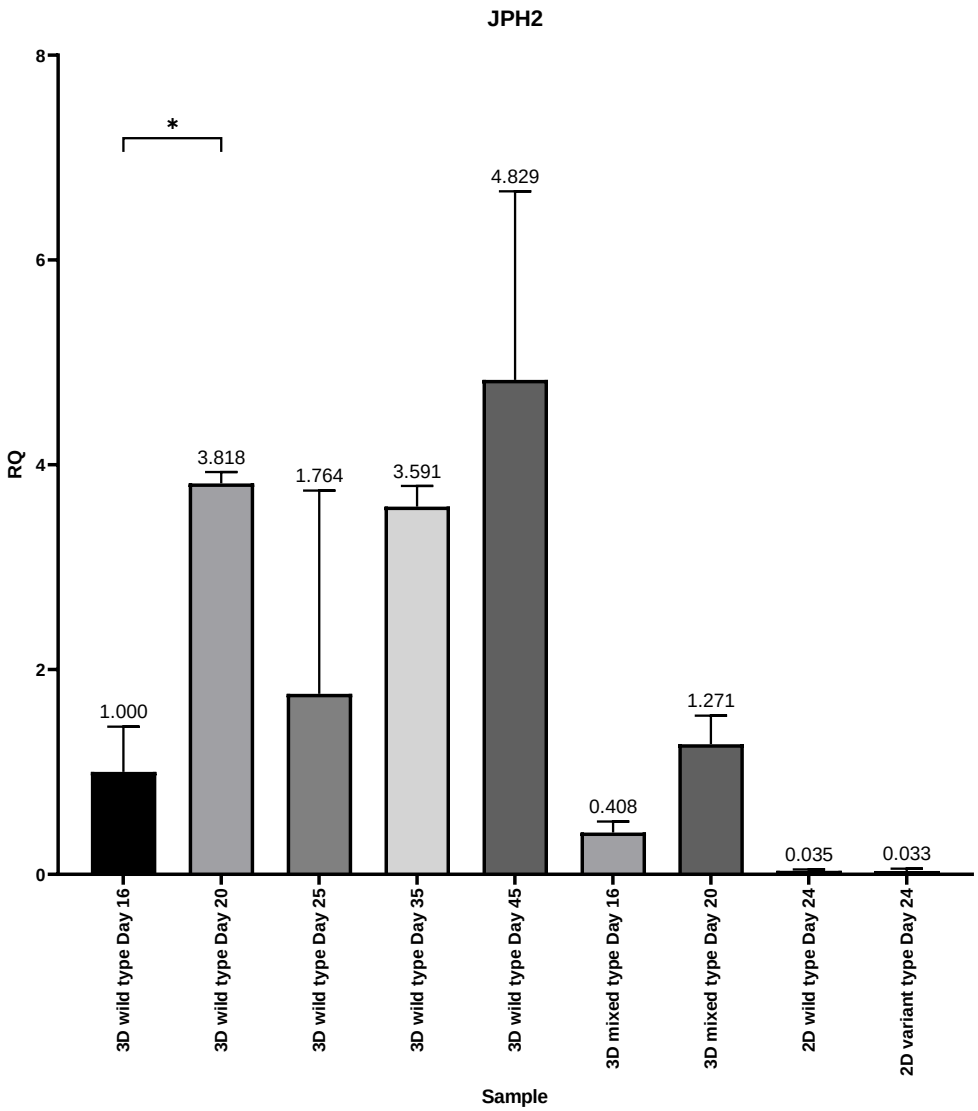

Fig.23 Comparison of *JPH2* expression in 2D and 3D samples at different time points. 3D wild type has higher *JPH2* expression level than mixed type, suggesting that 3D treatment can promote the maturation of wild type, and hypertrophic cardiomyopathy is also associated with the downregulation of this gene. The significant difference ($p<0.05$) between Day 16 and Day 20 shows that 3D wild type has a faster developmental rate.

KCNJ4 is associated with potassium channels (Li et al.), and it can be seen from Fig.24 that the 3D wild type has much higher expression than the mixed type and 2D samples, which indicates that the 3D wild type samples are more mature.

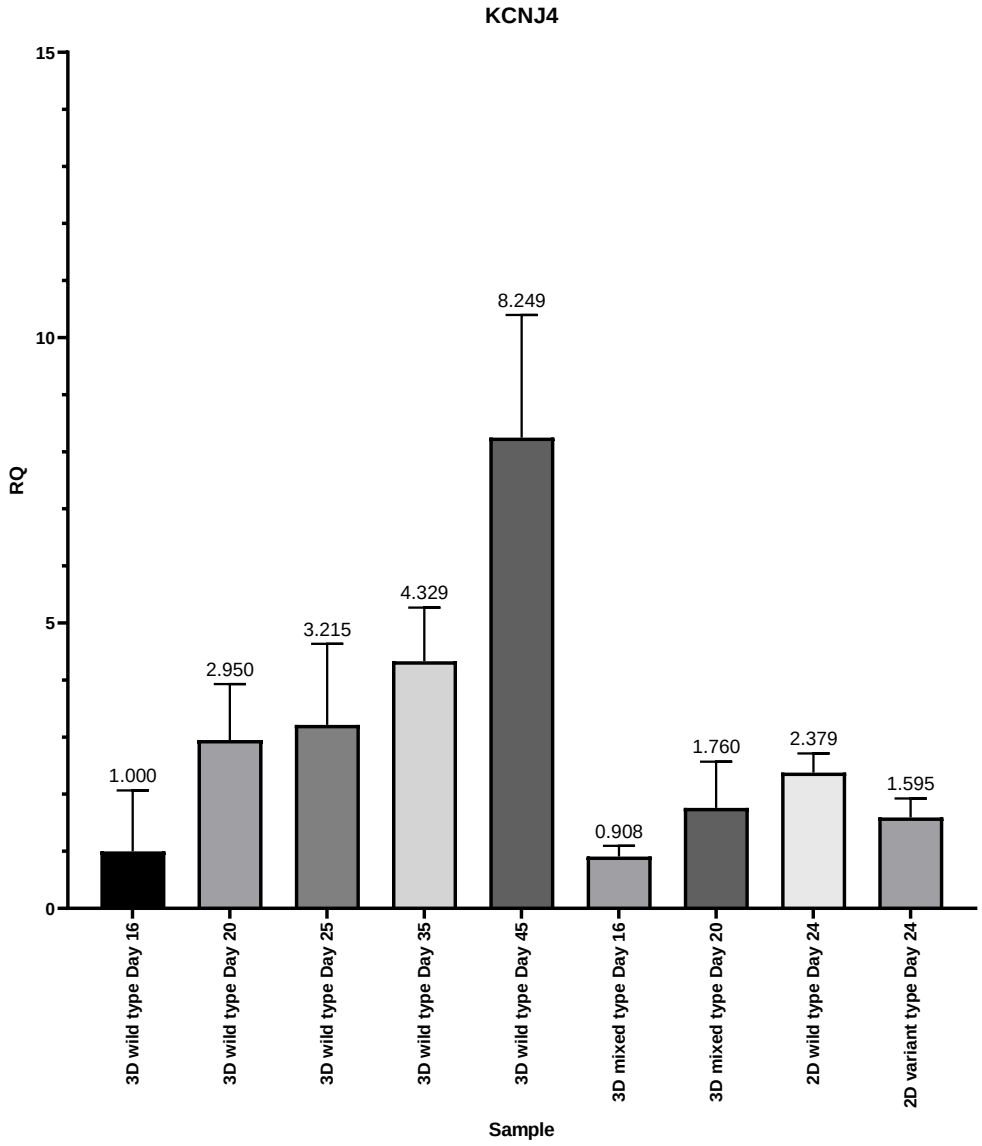

Fig.24 Comparison of *KCNJ4* expression in 2D and 3D samples at different time points. The expression of *KCNJ4* marks the maturity of cell development, and the expression of *KCNJ4* is much higher in 3D wild type than in mixed type, indicating that wild type has higher cell maturity.

MYH6 is associated with the formation of myosin. In Fig.25, we can see that there is a significant difference between Day 16 and Day 20 for the 3D wild type and another significant difference between Day 20 for the 3D wild type and Day 20 for the 3D mixed type, indicating that the 3D wild type rapidly expresses *MYH6* and therefore it is easy to see clearer sarcomeres in the 3D wild type samples. *MYH6* has

been shown to be significantly associated with HLHS (Kim et al., 2020; Tomita-Mitchell et al., 2016). In our results 3D mixed type exhibits much lower *MYH6* expression than healthy cells, demonstrating that mixed type contains a large number of cardiomyocytes with HLHS.

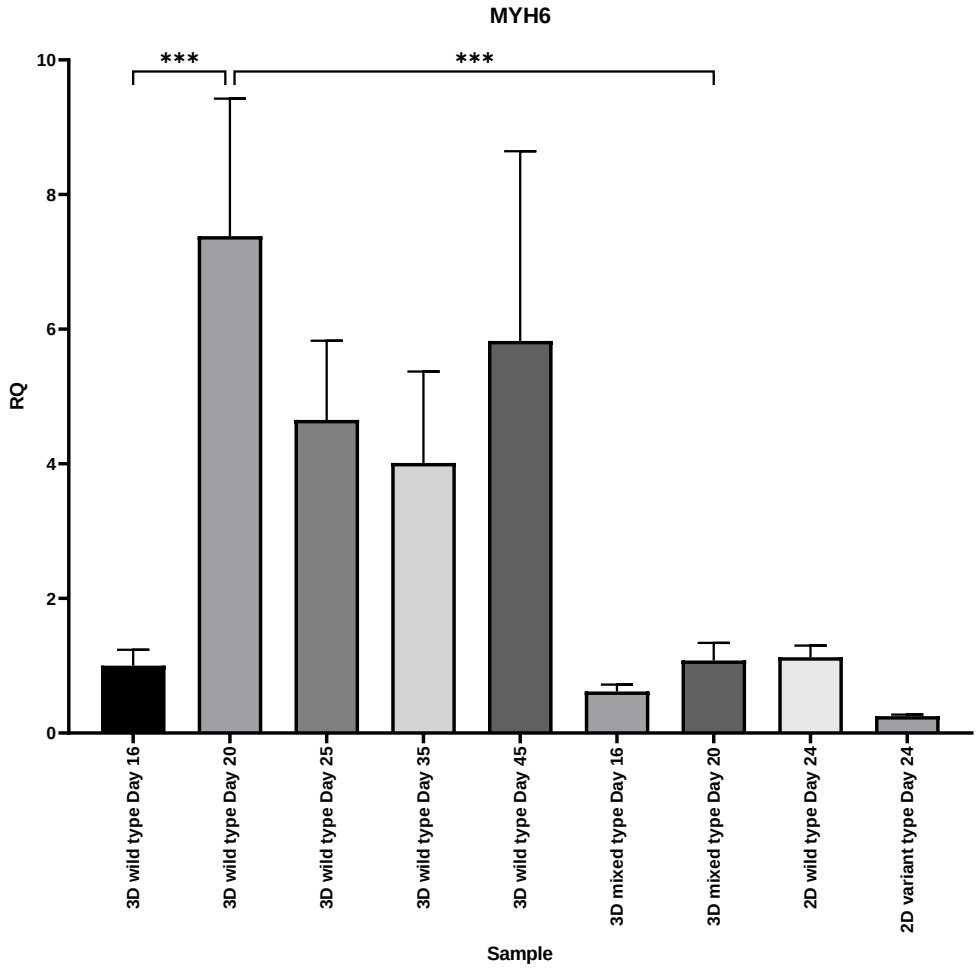

Fig.25 Comparison of *MYH6* expression in 2D and 3D samples at different time points. *MYH6* is responsible for encoding myosin, the significant difference between 3D wild type Day 16 and Day 20 shows that the 3D wild type has a more rapid developmental rate. The significant difference ($p<0.0005$) of the expression of *MYH6* between the 3D wild and the 3D mixed type suggesting that the samples in the 3D wild type have a clearer sarcomere structure. It is also demonstrated that the 3D mixed type contains cardiomyocytes with HLHS.

MYH7 plays an important role in the contraction of the heart, and the 3D samples shows higher *MYH7* expression levels (Fig.26), while the wild type in the 3D samples shows an increase compared with the mixed type, indicating that the wild type has a contractile advantage over the mixed type. It also shows that the wild type is more mature and ventricular like than the mixed type.

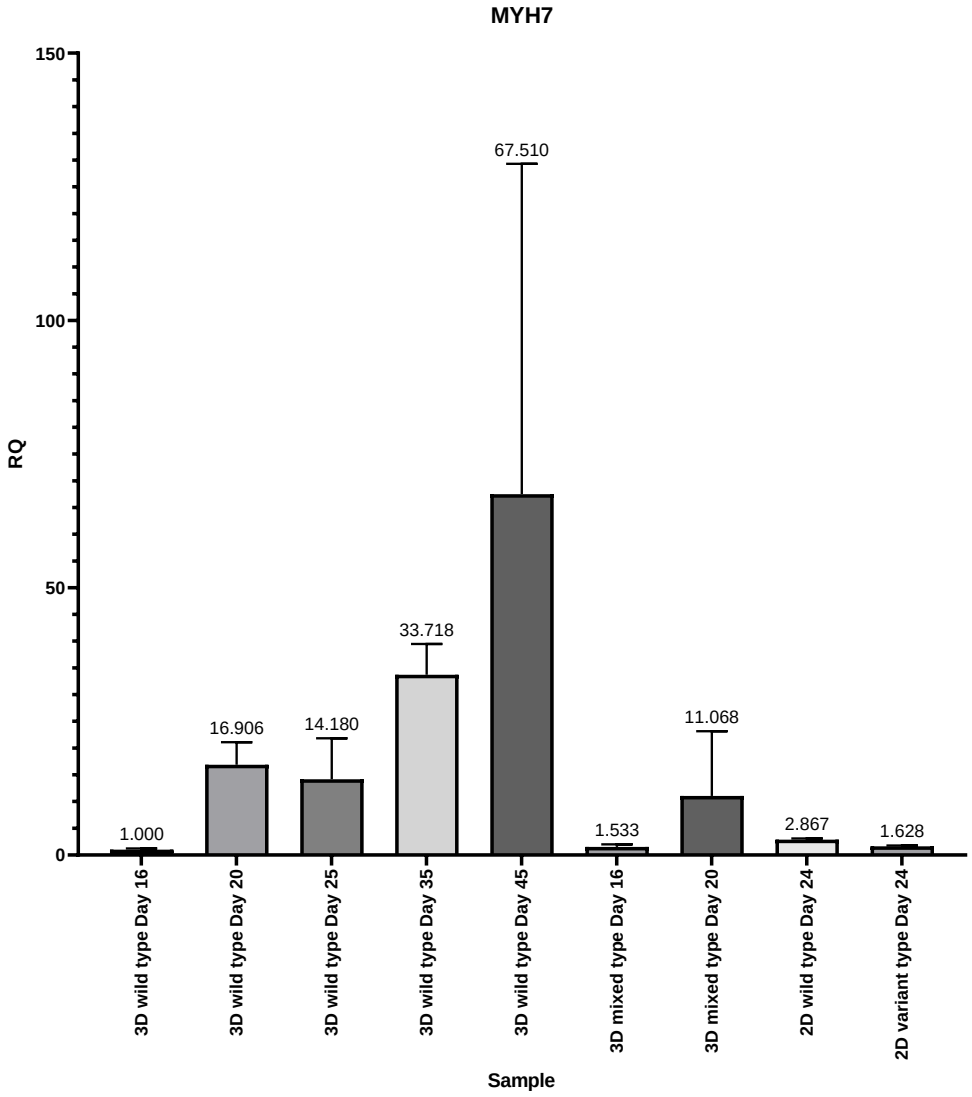

Fig.26 Comparison of *MYH7* expression in 2D and 3D samples at different time points. *MYH7* expression is associated with the contractility of cardiomyocytes. 3D wild type samples have higher *MYH7* expression than 3D mixed type, indicating that the wild type is more mature and contractile.

MYL7 is mainly responsible for regulating cardiac development and contractility, and the wild type in 3D samples has higher *MYL7* expression levels than the mixed type (Fig.27), suggesting that the wild type is more mature and more contractile. It is also reported that downregulation of *MYL7* is associated with structural changes in the heart (Sun et al., 2022).

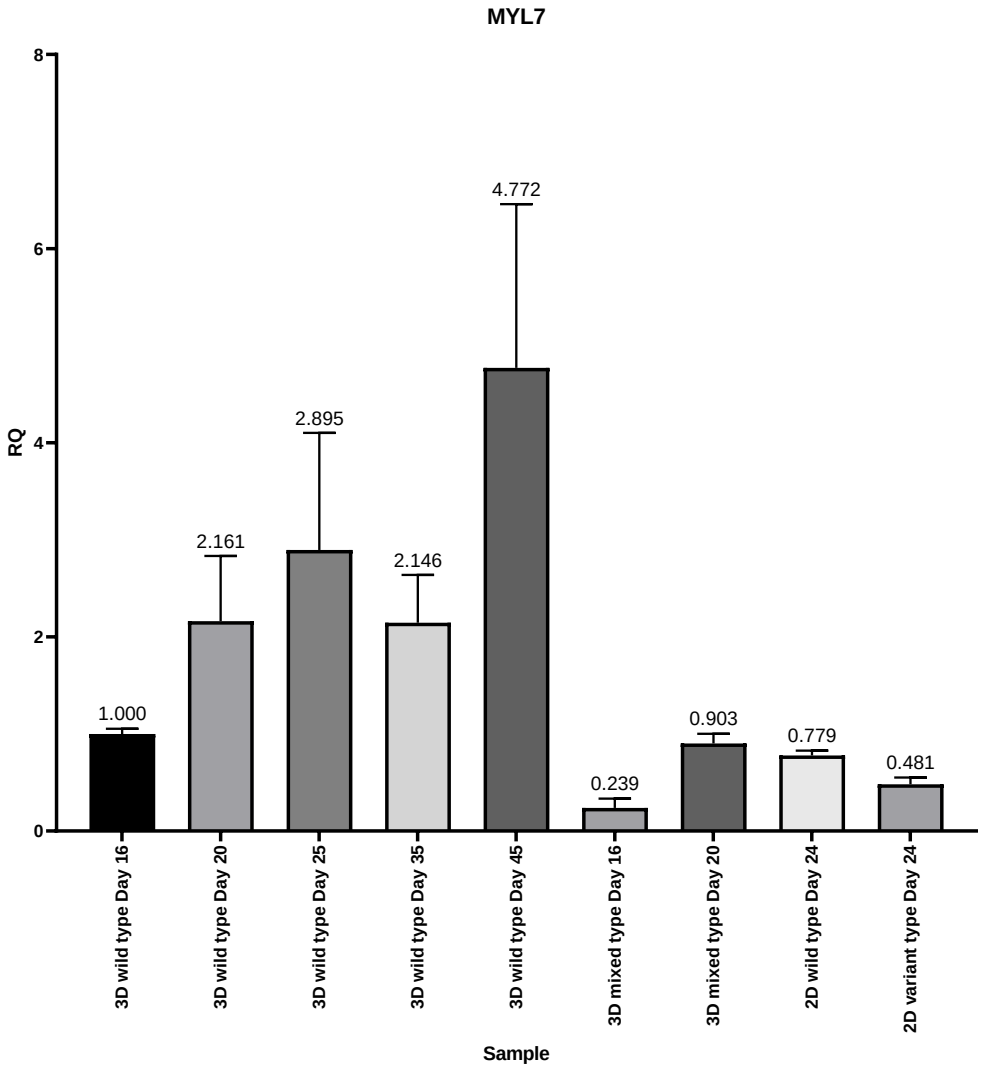

Fig.27 Comparison of *MYL7* expression in 2D and 3D samples at different time points. The expression of *MYL7* shows that the 3D wild type is more mature and

contractile, and the downregulation of this gene is also associated with structural changes in the heart.

4. Discussion

According to a statistic from 2010-2014, 1353 out of 10,000 babies investigated by researchers had HLHS (Mai et al., 2019). HLHS is congenital heart disease with a high mortality rate, and even after staged surgery, it does not have a 100% survival rate and is associated with a variety of morbidities that undoubtedly have multiple adverse effects on the patient. Research is increasingly looking for new treatments for HLHS, but both drugs and gene editing require the creation of tissue models (Wang et al., 2018b) that represent the structural and functional features of the heart.

The first step in constructing a tissue model in vitro is cell culture, which is traditionally done in 2D. However, almost all cells in the human body are surrounded by other cells and extracellular matrix (ECM) in a three-dimensional (3D) manner (Edmondson et al., 2014b), so in our study if we also cultured cardiomyocytes in 2D, these cells tended to adhere to the plate resulting in failure to form 3D structures (Duval et al., 2017b).

Also, the laminin in our bioink is the most powerful ECM enhancer for cardiomyocyte maturation (Chanthra et al., 2020), and laminin can promote cardiomyocyte alignment and enhance cardiomyocyte contractility (Mcdevitt et al., 2002; Ribeiro et al., 2014).

The major difference between our culture method and traditional 2D culture is crosslinking. We use UV light irradiation and crosslinking agent immersion to achieve a perfect crosslinking effect, allowing our samples to be suspended in the culture

medium. This allows each cell in the print to be immersed in the culture medium, creating growth conditions that fully mimic the in vivo environment.

The 3D printing technology allows for the precise layer-by-layer placement of bioink containing cells to create complex composite tissue structures. Each cell can be in an in vivo-like growth environment surrounded by other cells and ECM.

Through our study we found that bioengineered tissue models printed from iPSC-CMs were able to reproduce the activity of cardiomyocytes well in vitro. Samples in the wild type usually show regional contraction within 2-4 days after printing i.e., only a portion of the bioprinted tissue contracts. This contraction is very visible and can be observed with the naked eye (Fig.28). Most of the samples will gradually change from regional to global contraction (the printed tissue contracts as a whole) during subsequent culture (approximately 5-8 days after printing). Compared to the wild type, the mixed type tends to require a longer culture time (3-5 days) before regional contraction is observed. At the same time, samples in the mixed type tend not to show global contraction.

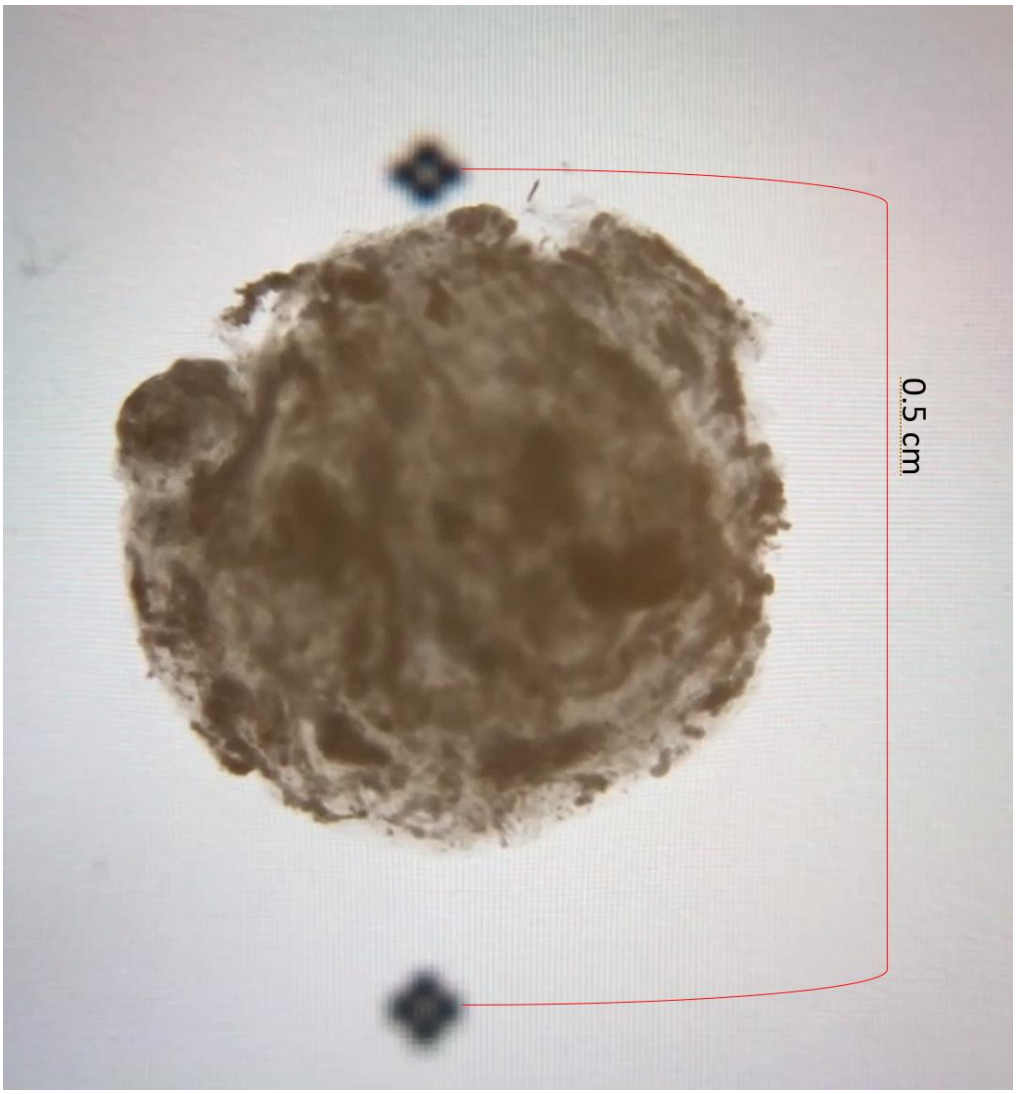

Fig.28 A frame from a video of a printed-out wild construct contraction taken with a cell phone (3× magnification).

Since the video analysis program we use is used to determine the maximal averaged displacement for each frame in the video, i.e., the displacement of each pixel is added together and then averaged for each pixel. Integral contraction produces a larger range of displacement, so samples in the wild type tend to have a larger displacement than the mixed type. This method does not reflect the experimental variability, as we fixed the frame rate of the video shots, each at 5 frames per second, with a timestep of 0.2 seconds. This resulted in the measurement of the contraction

velocity obtaining almost the same results as the displacement, despite the different displacements demonstrated for each sample, due to the step length limitation. We would like to point out that the results for displacement are more reliable than those for velocity. This method does not actually calculate the contraction velocity produced by the complete contraction, but we did not find a method that could achieve this calculation with automation, which is one of the goals of our subsequent research.

Both sarcomere length and organization index are the criteria we used to judge the maturity of our samples. In the results of sarcomere length, it can be seen that the wild type grows rapidly until Day 10, then slows down and reaches a maximum on Day 30. The mixed type also has a rapid growth rate until Day 10 but starts to decline after Day 10. Combined with the maximal displacement we calculated, the results of these two analyses are very consistent. Therefore, we hypothesize that at about 10 days after printing (approximately 25 days after differentiation) the cardiomyocytes with disease reach their maximal development, while the healthy cells have a longer developmental time.

In our study, organization index was used as another indicator to determine the degree of development of cardiomyocytes and alignment. It is higher in wild type than in mixed type for the same culture time. Mixed type reaches a maximum on Day 10 and then decreases, in agreement with our previous results for maximal displacement, maximal velocity and sarcomere length. The maximum value of the wild type is reached on Day 20 and decreases slightly on Day 30, in agreement with the previous analysis.

The RT-qPCR results show that the cells looked more mature (*JPH2*, *MYH7*, *KCNJ4*) and ventricle-like (*MYL2*, *MYH7*) in the 3D printed samples, and there are also significant differences between the wild type and the mixed type. In general, the RT-qPCR results are consistent with previous measurements, and the 3D processed samples has the advantages of faster development and greater contractility than the conventional 2D samples. They also show the difference in gene expression between healthy and diseased donors, a feature that is important for future research on effective treatment of HLHS.

Also, we found that the expression level of MYH6 in mixed type at Day 16 is about half of that in wild type, which is consistent with the fact that we had only half of the healthy cardiomyocytes of wild type in mixed type at the time of cell preparation. However, the difference in expression levels between the two groups widens dramatically on Day 5, and no longer shows the relationship that the mixed type is half of the wild type. Our hypothesis is that the diseased cardiomyocytes in the mixed type are damaging the healthy cells and disrupting the protein expression so that the healthy half of the cardiomyocytes do not express at the level they should. A similar situation occurs with the expression of *JPH2*.

Although our study successfully showed the difference between healthy and disease-carrying cardiomyocytes in vitro culture, we have many shortcomings, such as the number of samples is too small, the sample culture time is not long enough, and the method of analyzing data is not comprehensive enough. We measured the length of wild type cardiomyocytes to be more than 100 μm, corresponding to 100 to 150 μm

in other studies. However, we did not measure the length of cardiomyocytes in the mixed type because it was difficult to find well-structured sarcomeres in the mixed type. Also, we did not measure the heart rate of the printed heart tissue, which is an important indicator to compare the difference between healthy and disease-carrying, and we will include it in the subsequent experiments. We will continue to modify our protocol and add other tests such as drug tests in subsequent studies to make this model more informative.

The innovation and importance of our study is to simulate the growth environment of cardiomyocytes in the human body, substantially eliminating the differences caused by external factors such as culture and reflecting only the differences between healthy and diseased cardiomyocytes themselves.

These differences are the expression of the differences between healthy people and HLHS patients. If we can improve the performance of the disease-carrying model by some medical means, perhaps we can apply the same approach to the treatment of patients. But we still have a long way to go before we can achieve this. We want to eliminate the differences in external factors, but we don't know if there are other factors besides the culture environment. Also, we may be able to improve the performance of disease-carrying cardiomyocytes in in vitro culture, but we have no way of knowing if the same means are applicable to humans.

Although there is still a long way to go between the establishment of a differential model and the discovery of a treatment, we have made a good foundation

for other researchers, and we hope that someday in the future someone will be able to refine the treatment of HLHS based on our model and bring it to patients.

5. Conclusion

Our study succeeded in building a model in vitro that can mimic the growth environment of cardiomyocytes in vivo, a model with the functional characterization and gene expression of cardiomyocytes and able to show the difference between healthy and disease-carrying cardiomyocytes. We hope that our research will inspire more scholars and bring more attention to the importance of 3D bioprinting in research and medicine and that we will continue to improve our less-than-perfect model so that this model can be a helpful tool in the future to study the treatment of patients with HLHS.

BIBLIOGRAPHY

[1] Barron DJ, Kilby MD, Davies B, Wright JG, Jones TJ, Brawn WJ. Hypoplastic left heart syndrome. Lancet. 2009 Aug 15;374(9689):551-64. doi: 10.1016/S0140-6736(09)60563-8. PMID: 19683641.

[2] Best KE, Miller N, Draper E, Tucker D, Luyt K, Rankin J. The Improved Prognosis of Hypoplastic Left Heart: A Population-Based Register Study of 343 Cases in England and Wales. Front Pediatr. 2021 Jul 6;9:635776. doi: 10.3389/fped.2021.635776. PMID: 34295856; PMCID: PMC8289898.

[3] Tabbutt S, Dominguez TE, Ravishankar C, Marino BS, Gruber PJ, Wernovsky G, Gaynor JW, Nicolson SC, Spray TL. Outcomes after the stage I reconstruction comparing the right ventricular to pulmonary artery conduit with the modified Blalock Taussig shunt. Ann Thorac Surg. 2005 Nov;80(5):1582-90; discussion 1590-1. doi: 10.1016/j.athoracsur.2005.04.046. PMID: 16242421.

[4] Feinstein JA, Benson DW, Dubin AM, Cohen MS, Maxey DM, Mahle WT, Pahl E, Villafañe J, Bhatt AB, Peng LF, Johnson BA, Marsden AL, Daniels CJ, Rudd NA, Caldarone CA, Mussatto KA, Morales DL, Ivy DD, Gaynor JW, Tweddell JS, Deal BJ, Furck AK, Rosenthal GL, Ohye RG, Ghanayem NS, Cheatham JP, Tworetzky W, Martin GR. Hypoplastic left heart syndrome: current considerations and expectations. J Am Coll Cardiol. 2012 Jan 3;59(1 Suppl):S1-42. doi: 10.1016/j.jacc.2011.09.022. Erratum in: J Am Coll Cardiol. 2012 Jan 31;59(5):544. PMID: 22192720; PMCID: PMC6110391.

[5] Wang Z, Lee SJ, Cheng HJ, Yoo JJ, Atala A. 3D bioprinted functional and contractile cardiac tissue constructs. Acta Biomater. 2018 Apr 1;70:48-56. doi: 10.1016/j.actbio.2018.02.007. Epub 2018 Feb 13. PMID: 29452273; PMCID: PMC6022829.

[6] Park, IH., Lerou, P., Zhao, R. *et al.* Generation of human-induced pluripotent stem cells. *Nat Protoc* **3,** 1180–1186 (2008). https://doi.org/10.1038/nprot.2008.92

[7] Karakikes I, Ameen M, Termglinchan V, Wu JC. Human induced pluripotent stem cell-derived cardiomyocytes: insights into molecular, cellular, and functional phenotypes. Circ Res. 2015 Jun 19;117(1):80-8. doi: 10.1161/CIRCRESAHA.117.305365. PMID: 26089365; PMCID: PMC4546707.

[8] Jiang Y, Habibollah S, Tilgner K, Collin J, Barta T, Al-Aama JY, Tesarov L, Hussain R, Trafford AW, Kirkwood G, Sernagor E, Eleftheriou CG, Przyborski S, Stojković M, Lako M, Keavney B, Armstrong L. An induced pluripotent stem cell model of hypoplastic left heart syndrome (HLHS) reveals multiple expression and functional differences in HLHS-derived cardiac myocytes. Stem

Cells Transl Med. 2014 Apr;3(4):416-23. doi: 10.5966/sctm.2013-0105. Epub 2014 Mar 3. PMID: 24591732; PMCID: PMC3973710.

[9] Edmondson R, Broglie JJ, Adcock AF, Yang L. Three-dimensional cell culture systems and their applications in drug discovery and cell-based biosensors. Assay Drug Dev Technol. 2014 May;12(4):207-18. doi: 10.1089/adt.2014.573. PMID: 24831787; PMCID: PMC4026212.

[10] Duval K, Grover H, Han LH, Mou Y, Pegoraro AF, Fredberg J, Chen Z. Modeling Physiological Events in 2D vs. 3D Cell Culture. Physiology (Bethesda). 2017 Jul;32(4):266-277. doi: 10.1152/physiol.00036.2016. PMID: 28615311; PMCID: PMC5545611.

[11] Murphy SV, Atala A. 3D bioprinting of tissues and organs. Nat Biotechnol. 2014 Aug;32(8):773-85. doi: 10.1038/nbt.2958. PMID: 25093879.

[12] Ozbolat IT, Hospodiuk M. Current advances and future perspectives in extrusion-based bioprinting. Biomaterials. 2016 Jan;76:321-43. doi: 10.1016/j.biomaterials.2015.10.076. Epub 2015 Oct 31. PMID: 26561931.

[13] GhavamiNejad A, Ashammakhi N, Wu XY, Khademhosseini A. Crosslinking Strategies for 3D Bioprinting of Polymeric Hydrogels. Small. 2020 Sep;16(35):e2002931. doi: 10.1002/smll.202002931. Epub 2020 Jul 30. PMID: 32734720; PMCID: PMC7754762.

[14] Reddy N, Reddy R, Jiang Q. Crosslinking biopolymers for biomedical applications. Trends Biotechnol. 2015 Jun;33(6):362-9. doi: 10.1016/j.tibtech.2015.03.008. Epub 2015 Apr 14. PMID: 25887334.

[15] Derakhshanfar S, Mbeleck R, Xu K, Zhang X, Zhong W, Xing M. 3D bioprinting for biomedical devices and tissue engineering: A review of recent trends and advances. Bioact Mater. 2018 Feb 20;3(2):144-156. doi: 10.1016/j.bioactmat.2017.11.008. PMID: 29744452; PMCID: PMC5935777.

[16] Gao, G., Lee, J. H., Jang, J., Lee, D. H., Kong, J.-S., Kim, B. S., Choi, Y.-J., Jang, W. B., Hong, Y. J., Kwon, S.-M., Cho, D.-W., *Adv. Funct. Mater.* 2017, 27, 1700798. https://doi.org/10.1002/adfm.201700798

[17] Lian X, Bao X, Zilberter M, Westman M, Fisahn A, Hsiao C, Hazeltine LB, Dunn KK, Kamp TJ, Palecek SP. Chemically defined, albumin-free human cardiomyocyte generation. Nat Methods. 2015 Jul;12(7):595-6. doi: 10.1038/nmeth.3448. PMID: 26125590; PMCID: PMC4663075.

[18] Shradhanjali A, Riehl BD, Duan B, Yang R, Lim JY. Spatiotemporal Characterizations of Spontaneously Beating Cardiomyocytes with Adaptive Reference Digital Image Correlation. Sci Rep. 2019 Dec 5;9(1):18382. doi: 10.1038/s41598-019-54768-w. PMID: 31804542; PMCID: PMC6895104.

[19] Hinson JT, Chopra A, Nafissi N, Polacheck WJ, Benson CC, Swist S, Gorham J, Yang L, Schafer S, Sheng CC, Haghighi A, Homsy J, Hubner N, Church G,

Cook SA, Linke WA, Chen CS, Seidman JG, Seidman CE. HEART DISEASE. Titin mutations in iPS cells define sarcomere insufficiency as a cause of dilated cardiomyopathy. Science. 2015 Aug 28;349(6251):982-6. doi: 10.1126/science.aaa5458. PMID: 26315439; PMCID: PMC4618316.

[20] Deacon DC, Happe CL, Chen C, Tedeschi N, Manso AM, Li T, Dalton ND, Peng Q, Farah EN, Gu Y, Tenerelli KP, Tran VD, Chen J, Peterson KL, Schork NJ, Adler ED, Engler AJ, Ross RS, Chi NC. Combinatorial interactions of genetic variants in human cardiomyopathy. Nat Biomed Eng. 2019 Feb;3(2):147-157. doi: 10.1038/s41551-019-0348-9. Epub 2019 Feb 7. PMID: 30923642; PMCID: PMC6433174.

[21] Lundy SD, Zhu WZ, Regnier M, Laflamme MA. Structural and functional maturation of cardiomyocytes derived from human pluripotent stem cells. Stem Cells Dev. 2013 Jul 15;22(14):1991-2002. doi: 10.1089/scd.2012.0490. Epub 2013 Apr 5. PMID: 23461462; PMCID: PMC3699903.

[22] Yang X, Pabon L, Murry CE. Engineering adolescence: maturation of human pluripotent stem cell-derived cardiomyocytes. Circ Res. 2014 Jan 31;114(3):511-23. doi: 10.1161/CIRCRESAHA.114.300558. PMID: 24481842; PMCID: PMC3955370.

[23] Laing, Nigel G et al. “Mutations and polymorphisms of the skeletal muscle alpha-actin gene (ACTA1).” Human mutation vol. 30,9 (2009): 1267-77. doi:10.1002/humu.21059

[24] Ilkovski B, Clement S, Sewry C, North KN, Cooper ST. Defining alpha-skeletal and alpha-cardiac actin expression in human heart and skeletal muscle explains the absence of cardiac involvement in *ACTA1* nemaline myopathy. Neuromuscul Disord. 2005 Dec;15(12):829-35. doi: 10.1016/j.nmd.2005.08.004. Epub 2005 Nov 8. PMID: 16288873.

[25] Sheikh F, Lyon RC, Chen J. Functions of myosin light chain-2 (MYL2) in cardiac muscle and disease. Gene. 2015 Sep 10;569(1):14-20. doi: 10.1016/j.gene.2015.06.027. Epub 2015 Jun 12. Erratum in: Gene. 2015 Oct 15;571(1):151. PMID: 26074085; PMCID: PMC4496279.

[26] Tupling AR, Bombardier E, Gupta SC, Hussain D, Vigna C, Bloemberg D, Quadrilatero J, Trivieri MG, Babu GJ, Backx PH, Periasamy M, MacLennan DH, Gramolini AO. Enhanced Ca2+ transport and muscle relaxation in skeletal muscle from sarcolipin-null mice. Am J Physiol Cell Physiol. 2011 Oct;301(4):C841-9. doi: 10.1152/ajpcell.00409.2010. Epub 2011 Jun 22. PMID: 21697544; PMCID: PMC3654932.

[27] Babu GJ, Zheng Z, Natarajan P, Wheeler D, Janssen PM, Periasamy M. Overexpression of sarcolipin decreases myocyte contractility and calcium transient. Cardiovasc Res. 2005 Jan 1;65(1):177-86. doi: 10.1016/j.cardiores.2004.08.012. PMID: 15621045.

[28] Sakamuro D, Elliott KJ, Wechsler-Reya R, Prendergast GC. *BIN1* is a novel MYC-interacting protein with features of a tumour suppressor. Nat Genet. 1996 Sep;14(1):69-77. doi: 10.1038/ng0996-69. PMID: 8782822.

[29] Landstrom AP, Weisleder N, Batalden KB, Bos JM, Tester DJ, Ommen SR, Wehrens XH, Claycomb WC, Ko JK, Hwang M, Pan Z, Ma J, Ackerman MJ. Mutations in JPH2-encoded junctophilin-2 associated with hypertrophic cardiomyopathy in humans. J Mol Cell Cardiol. 2007 Jun;42(6):1026-35. doi: 10.1016/j.yjmcc.2007.04.006. Epub 2007 Apr 18. PMID: 17509612; PMCID: PMC4318564.

[30] Landstrom AP, Kellen CA, Dixit SS, van Oort RJ, Garbino A, Weisleder N, Ma J, Wehrens XH, Ackerman MJ. Junctophilin-2 expression silencing causes cardiocyte hypertrophy and abnormal intracellular calcium-handling. Circ Heart Fail. 2011 Mar;4(2):214-23. doi: 10.1161/CIRCHEARTFAILURE.110.958694. Epub 2011 Jan 7. PMID: 21216834; PMCID: PMC3059380.

[31] Li, Tao, et al. "Screening of potassium channel mutations in patients with atrial fibrillation."

[32] Kim MS, Fleres B, Lovett J, Anfinson M, Samudrala SSK, Kelly LJ, Teigen LE, Cavanaugh M, Marquez M, Geurts AM, Lough JW, Mitchell ME, Fitts RH, Tomita-Mitchell A. Contractility of Induced Pluripotent Stem Cell-Cardiomyocytes With an *MYH6* Head Domain Variant Associated With Hypoplastic Left Heart Syndrome. Front Cell Dev Biol. 2020 Jun 23;8:440. doi: 10.3389/fcell.2020.00440. PMID: 32656206; PMCID: PMC7324479.

[33] Tomita-Mitchell A, Stamm KD, Mahnke DK, Kim MS, Hidestrand PM, Liang HL, Goetsch MA, Hidestrand M, Simpson P, Pelech AN, Tweddell JS, Benson DW, Lough JW, Mitchell ME. Impact of *MYH6* variants in hypoplastic left heart syndrome. Physiol Genomics. 2016 Dec 1;48(12):912-921. doi: 10.1152/physiolgenomics.00091.2016. Epub 2016 Oct 27. PMID: 27789736; PMCID: PMC5206387.

[34] Sun J, Guo X, Yu P, Liang J, Mo Z, Zhang M, Yang L, Huang X, Hu B, Liu J, Ouyang Y, He M. Vasorin deficiency leads to cardiac hypertrophy by targeting *MYL7* in young mice. J Cell Mol Med. 2022 Jan;26(1):88-98. doi: 10.1111/jcmm.17034. Epub 2021 Dec 2. PMID: 34854218; PMCID: PMC8742182.

[35] Mai CT, Isenburg JL, Canfield MA, Meyer RE, Correa A, Alverson CJ, Lupo PJ, Riehle-Colarusso T, Cho SJ, Aggarwal D, Kirby RS; National Birth Defects Prevention Network. National population-based estimates for major birth defects, 2010-2014. Birth Defects Res. 2019 Nov 1;111(18):1420-1435. doi: 10.1002/bdr2.1589. Epub 2019 Oct 3. PMID: 31580536; PMCID: PMC7203968.

[36] Wang Z, Lee SJ, Cheng HJ, Yoo JJ, Atala A. 3D bioprinted functional and contractile cardiac tissue constructs. Acta Biomater. 2018 Apr 1;70:48-56. doi: 10.1016/j.actbio.2018.02.007. Epub 2018 Feb 13. PMID: 29452273; PMCID: PMC6022829.

[37] Edmondson R, Broglie JJ, Adcock AF, Yang L. Three-dimensional cell culture systems and their applications in drug discovery and cell-based biosensors. Assay Drug Dev Technol. 2014 May;12(4):207-18. doi: 10.1089/adt.2014.573. PMID: 24831787; PMCID: PMC4026212.

[38] Duval K, Grover H, Han LH, Mou Y, Pegoraro AF, Fredberg J, Chen Z. Modeling Physiological Events in 2D vs. 3D Cell Culture. Physiology (Bethesda). 2017 Jul;32(4):266-277. doi: 10.1152/physiol.00036.2016. PMID: 28615311; PMCID: PMC5545611.

[39] Chanthra N, Abe T, Miyamoto M, Sekiguchi K, Kwon C, Hanazono Y, Uosaki H. A Novel Fluorescent Reporter System Identifies Laminin-511/521 as Potent Regulators of Cardiomyocyte Maturation. Sci Rep. 2020 Mar 6;10(1):4249. doi: 10.1038/s41598-020-61163-3. PMID: 32144297; PMCID: PMC7060274.

[40] McDevitt TC, Angello JC, Whitney ML, Reinecke H, Hauschka SD, Murry CE, Stayton PS. In vitro generation of differentiated cardiac myofibers on micropatterned laminin surfaces. J Biomed Mater Res. 2002 Jun 5;60(3):472-9. doi: 10.1002/jbm.1292. PMID: 11920672.

[41] Ribeiro AJ, Zaleta-Rivera K, Ashley EA, Pruitt BL. Stable, covalent attachment of laminin to microposts improves the contractility of mouse neonatal cardiomyocytes. ACS Appl Mater Interfaces. 2014 Sep 10;6(17):15516-26. doi: 10.1021/am5042324. Epub 2014 Aug 26. PMID: 25133578; PMCID: PMC4160263.

APPENDIX

A. Preparation of bioink and cells

1. Preheat the beads, media, trypsin and bioink approximately 30 minutes prior to start.
2. Aspirate the medium, add 1 ml of PBS solution to wash the cells then aspirate the PBS solution.
3. Add 1 ml of 0.25% trypsin and incubate at 37 degrees C for 10 minutes.
4. The cells were separated in trypsin by several aspirations with a pipette.
5. Collect cells and add double amount of RPMI/20% FBS solution and mix well by inverting tube.
6. Take 10ul and count the cells using a Biorad cell counter.
7. Centrifuge at 1000 rpm for 5 minutes.
8. During centrifugation, a blunt forceps is used to connect the syringe to the tubing.
9. Take the ink warmed at 37 degrees, connect the syringe, push the ink tube with blunt forceps and transfer 0.8 ml of ink to the syringe.
10. Take the centrifuged cells, aspirate the supernatant off and take the cell pellet.
11. Resuspend the cells in 0.2 ml of medium.
12. Add 1µl of 5 µM Rock inhibitor to the cells.
13. Add the cells to bioink.

14. Connect a new 3 ml syringe to the cell + bioink syringe and mix, pushing the syringe back and forth 10 times to distribute the cells evenly in the ink.
15. Remove empty syringe.
16. Place the stopper in the syringe to be used for printing and connect it to the syringe containing the cell and ink mixture and fill the new syringe with ink + cells.
17. Seal the top and bottom of the syringe to be used for printing with the caps.
18. Centrifuge the syringe at 1000 rpm for 5 minutes.
19. Remove excessive bubbles.
20. Put prepared ink+cells in the 37 degrees warmed up beads.
21. Before printing, the ink + cells are incubated at 25 degrees for 10 minutes to cool down to the temperature required for printing.

B. Protocol for bioprinting

1. Turn on bioprinter.
2. Under Utilities menu, change printheads to 25°C.
3. Under Utilities menu, set airflow to 15.
4. Calibrate both pressure gauges by depressing both gray buttons on each display simultaneously for a few seconds. Display will zero out.
5. Turn on compressor. Syringe holder should move up.
6. Set syringe #1 and syringe #2 pressure to zero using valves on right side of printer. Pull out each knob, adjust and push back in to lock.

7. Place calibration syringe into the holder and under Prepare Bioprinting on main screen select Home Axes.
8. Syringe holder will pop down and locate the origin for printing.
9. Place waste plate and move z to +8.
10. Calibrate z.
11. Remove plate and calibration syringe.
12. Spray surface underneath printing tray thoroughly with 70% EtOH and wipe clean.
13. Secure syringe in holder and make sure it is all the way down, place the waste plate.
14. Under Prepare Bioprint, select Turn on Printhead 1 and slowly adjust pressure until ink is flowing smoothly (around 18kPa).
15. Turn off Printhead 1.
16. Under main menu, Bioprint, select code (4×4×0.6mm) that was loaded for the specific print job.
17. After the previous plate is printed, replace it with a new plate.
18. Remove syringe (with bioink and cells) and dispose of in biohazard.
19. Dial printhead pressures back to 0.
20. Turn off air compressor.
21. Press valve on back of compressor to release air.
22. Turn off bioprinter.

23. All biohazards must be placed in biohazard trashcan. No open bags can be left overnight for safety reasons.
24. Use cavicide to clean all surfaces inside the bioprinter.
25. Use cavicide to clean all lab bench surfaces surrounding bioprinter.

C. Protocol for immunofluorescence staining

1. Drain as much medium off as possible.
2. Gently rinse the 3D constructs at least 3 times with 1× PBS.
3. Fix the 3D constructs with 4% PFA and shake them at -4 degrees C for 15 minutes.
4. Wash with PBS 3 times.
5. Permeabilize with 0.2% Triton/PBS solution and shake for 15 minutes to disrupt the membrane.
6. Remove Triton/PBS solution.
7. Apply the primary antibodies together in PBS overnight at the 4 degrees C by rocking with following concentrations:
    a. Apply GATA4 at a 1:400.
    b. Apply α-actinin at a 1:250 dilution.
8. Remove the primary antibodies and rinse 4 times with PBS.
9. Apply the secondary antibodies together in PBS for 1 hour at room temperature using a dilution for both of 1:750 and DAPI at the same dilution:
    a. Donkey anti-Rabbit Alexa Fluor 594.

b. Goat anti-Mouse IgG1 Alexa Fluor 488.

c. DAPI.

10. Thoroughly wash out the secondary antibodies using 1x PBS.

11. Mount a coverslip over cells using Prolong Gold Antifade regent.

D. Protocol for organization index measurement

1. Select the image you want to measure the organization index, if it is a multi-color image, you can separate the colors in ImageJ, the operation is as follows: Image, Color, Split Channels, then Process, Binary, Make Binary; if it is a single-color image, directly Image□Type□8-bit, then Process, Binary, Make Binary.

2. The processed image will be Analyze, Tools, Grid, you can freely choose the size of Area per point, the default value is 51782 pixels^2.

3. Select Straight Line in the toolbar and draw a straight line through the sarcomeres along their alignment in the grid.

4. Use CTRL + K after drawing the line, get the intensity table.

5. Click Data, Copy All Data at the bottom of the table, then create a new Text Document in the folder you like, and name it with a number, then paste the copied data in it. For example, the TXT file named '1' contains the data copied from the first grid, the TXT file named '2' contains the data copied from the second grid, and so on.

6. After you have stored all the grid data in the TXT file, open MATLAB and use the following code you will get the organization index of each grid.

```
clear all
cd('C:\Users\Auster\Desktop\new\4.22 p2d10');% The location
where you store your data
for k=8:9;%The number of the TXT file you want to analyze
   myfilename = sprintf('%d.txt', k);

mydata{k} = importdata(myfilename);

y_1 = cell2mat(mydata(k)); %Import Region of Interest
intensity .txt file

y = y_1.data;

y = mydata{1,k}.data(:,2);

z = fftshift(fft(y));

rawpowerspec=abs(z).^2;

powerspecnorm=(rawpowerspec)./(max(max(rawpowerspec)));

pks = findpeaks(powerspecnorm);

b = sort(pks);

c = length(b);

d(k) = b(c-1);

end
```

E. Protocol for sarcomere length measurement

1. Choose and open the image you want to measure in ImageJ.
2. Enlarge the scale bar, use the straight-line tool to draw a line from the beginning to the end of the scale.
3. Click Analyze then Set Scale, fill in the actual length in the Known distance, change the unit to the actual unit.
4. You will get a value in unit of pixels/μm, then you need to calculate the length of each pixel.
5. Choose the same image you opened in ImageJ, then open it in ZEN software.

6. Select Profile in the left toolbar, then click Rectangle.
7. Enlarge the area of interest, use mouse to draw a rectangle perpendicular to the sarcomeres.
8. You will get an intensity plot of the sarcomeres within the rectangle you drew.
9. Measure the pixel distance between peaks.
10. Multiply the distance with the ratio you got from ImageJ.